A&A 677, A15 (2023)
https://doi.org/10.1051/0004-6361/202245277

Astronomy & Astrophysics

The GUAPOS project

III. Characterization of the O- and N-bearing complex organic molecules content and search for chemical differentiation⋆

C. Mininni[1], M. T. Beltrán[2], L. Colzi[3], V. M. Rivilla[3], F. Fontani[2], A. Lorenzani[2], Á. López-Gallifa[3], S. Viti[4,5], Á. Sánchez-Monge[6,7,8,9], P. Schilke[9], and L. Testi[10]

[1] INAF – IAPS, Via del Fosso del Cavaliere 100, 00133 Roma, Italy
e-mail: chiara.mininni@inaf.it
[2] INAF – Osservatorio Astrofisico di Arcetri, Largo E. Fermi 5, 50125 Firenze, Italy
[3] Centro de Astrobiología (CSIC, INTA), Ctra. de Ajalvir, km. 4, Torrejón de Ardoz, 28850 Madrid, Spain
[4] Leiden Observatory, Leiden University, Huygens Laboratory, Niels Bohrweg 2, 2333 CA Leiden, The Netherlands
[5] Department of Physics and Astronomy, University College London, Gower Street, WC1E 6BT, London, UK
[6] Institut de Ciéncies de l'Espai (ICE, CSIC), Can Magrans s/n, 08193, Bellaterra, Barcelona, Spain
[7] Institut d'Estudis Espacials de Catalunya (IEEC), Barcelona, Spain
[8] Observatorio Astronómico Nacional (OAN), Alfonso XII, 3 28014, Madrid, Spain
[9] I. Physikalisches Institut, Universität zu Köln, Zülpicher Str. 77, 50937 Köln, Germany
[10] Dipartimento di Fisica e Astronomia, Universitá di Bologna, Via Gobetti 93/2, 40122 Bologna, Italy

Received 24 October 2022 / Accepted 16 June 2023

ABSTRACT

Context. The G31.41+0.31 Unbiased ALMA sPectral Observational Survey (GUAPOS) project targets the hot molecular core (HMC) G31.41+0.31 (G31) to reveal the complex chemistry of one of the most chemically rich high-mass star-forming regions outside the Galactic center (GC).

Aims. In the third paper of the project we present a study of nine O-bearing (CH_3OH, $^{13}CH_3OH$, $CH_3^{18}OH$, CH_3CHO, CH_3OCH_3, CH_3COCH_3 , C_2H_5OH, aGg′-$(CH_2OH)_2$, and gGg′-$(CH_2OH)_2$) and six N-bearing (CH_3CN, $^{13}CH_3CN$, $CH_3^{13}CN$, C_2H_3CN, C_2H_5CN, and $C_2H_5^{13}CN$) complex organic molecules toward G31. The aim of this work is to characterize the abundances in G31 and to compare them with the values estimated in other sources. Moreover, we searched for a possible chemical segregation between O-bearing and N-bearing species in G31, which hosts four compact sources as seen with higher angular resolution data. In the discussion we also include the three isomers of $C_2H_4O_2$ and the O- and N-bearing molecular species NH_2CHO, CH_3NCO, $CH_3C(O)CH_2$, and CH_3NHCHO, which were analyzed in previous GUAPOS papers.

Methods. Observations were carried out with the interferometer ALMA and cover the entire Band 3 from 84 to 116 GHz (∼32 GHz bandwidth) with an angular resolution of 1.2″ × 1.2″ (∼4400 au × 4400 au) and a spectral resolution of ∼0.488 MHz (∼1.3–1.7 km s^{-1}). The transitions of the 14 molecular species were analyzed with the tool SLIM of MADCUBA to determine the physical parameters of the emitting gas. Moreover, we analyzed the morphology of the emission of the molecular species.

Results. The values of abundances with respect to H_2 in G31 range from 10^{-6} to 10^{-10} for the different species. We compared the abundances with respect to methanol of O-bearing, N-bearing, and O- and N-bearing COMs in G31 with 27 other sources, including other hot molecular cores inside and outside the GC, hot corinos, shocked regions, envelopes around young stellar objects, and quiescent molecular clouds, and with chemical models.

Conclusions. From the comparison with other sources there is not a unique template for the abundances in hot molecular cores, pointing toward the importance of the thermal history for the chemistry of the various sources. The abundances derived from the chemical models are in good agreement, within a factor of 10, with those of G31. From the analysis of the maps we derived the peak positions of all the molecular species toward G31. Different species peak at slightly different positions, and this, together with the different central velocities of the lines obtained from the spectral fitting, point to chemical differentiation of selected O-bearing species.

Key words. astrochemistry – line: identification – stars: formation – ISM: molecules – instrumentation: interferometers – ISM: individual objects: G31.41+0.31

1. Introduction

The spectrum of hot molecular cores (HMCs) reveals a very rich chemistry with many rotational transitions of a large number of molecular species, including complex organic molecules (COMs), which are molecules containing carbon with six or more atoms (Herbst & van Dishoeck 2009). These regions are associated with an evolved phase of high-mass star formation, when a protostellar object has already formed in the core, leading to an increase in the temperature to a few hundred K. The high temperatures (>100 K) reached in HMCs cause the release (by thermal desorption) of the products of the grain-surface

⋆ Tables C.1–C.15 are only available at the CDS via anonymous cdsarc.cds.unistra.fr (130.79.128.5) or via https://cdsarc.cds.unistra.fr/viz-bin/cat/J/A+A/677/A15

reactions into the gas-phase. Furthermore, the presence of shocks can also lead to the release in gas-phase of COMs (e.g., Palau et al. 2011). The study of these regions is important to reveal the chemistry that occurs during the star formation process and to constrain the chemical pathways responsible for the abundance variations of several species under the physical conditions present in these cores.

The abundances of chemical species in HMCs are influenced by several factors, for example the physical conditions of the gas (density n, and temperature T), cosmic-rays (CR) flux, age of the embedded source, external heating, and protostellar outflows that produce shocked regions (e.g., Garrod 2013; Sipilä et al. 2021). Inhomogeneities in each of these factors can potentially favor, or inhibit, the chemical processes responsible for the formation of different species in different regions of the source. Ultimately, this could also produce chemical differentiation, where the abundances of some molecular species are enhanced in some regions, while others are less abundant (or have such low abundances that they are not detected).

As an example, Blake et al. (1987) found spatial segregation between N-bearing molecules and O-bearing molecules toward Orion-KL, the closest high-mass star-forming region. In their study the emission of N-bearing molecules was detected toward the hot core, while the O-bearing species were detected toward the compact ridge. This was confirmed by further single-dish and interferometric studies (e.g., Friedel & Snyder 2008; Crockett et al. 2015). However, this simple distinction does not provide the full picture. Several studies have shown that some O-bearing molecular species, such as acetone (CH_3COCH_3), are more co-spatial to N-bearing species than to other O-bearing species, and also among O-bearing species the emitting regions vary (e.g., Widicus Weaver & Friedel 2012; Peng et al. 2013; Feng et al. 2015; Tercero et al. 2018). Tercero et al. (2018) concluded that among O-bearing molecules in Orion-KL, spatial segregation is observed between molecules containing a C–O–C bond and those containing a C–O–H bond. The strong chemical differentiation seen in this source could be a peculiar case caused by an explosive event in the central region of Orion (e.g., Bally & Zinnecker 2005; Bally et al. 2017), as also indicated by the elongated emission of several molecular species observed by Pagani et al. (2019). However, the chemical differentiation observed in Orion-KL seems to be not unique. Chemical differentiation has also been observed toward other high-mass star-forming regions. Wyrowski et al. (1999), Remijan et al. (2004), Kalenskii & Johansson (2010), Zernickel et al. (2012), Allen et al. (2017),van der Walt et al. (2021), and Peng et al. (2022) observed chemical differentiation between O-bearing and N-bearing molecules toward W3(OH), W51 e1/e2, W75N, G19.61-0.23, NGC 6334I, G35.20-0.74N, CygX-N30 (W75N B), and G9.62+0.19 (especially between core MM8 and MM4), respectively, while Jiménez-Serra et al. (2012) found chemical segregation of selected species in AFGL2591. Jiménez-Serra et al. (2016) also detected chemical differentiation in the cold prestellar core L1544. Bøgelund et al. (2019) have shown that in the high-mass star-forming region AFGL4176 the peak of the emission of O-bearing molecules is offset 0.2″ from the peak of N-bearing species, and that the mean excitation temperature is higher for N-bearing than for O-bearing species: ∼120–160 K for O-bearing and ∼190–240 K for N-bearing species. A higher excitation temperature of N-bearing species with respect to O-bearing species was also reported by Widicus Weaver et al. (2017) from the analysis of the spectra of 30 star-forming regions, half of which were HMCs. Recently, Qin et al. (2022) reported a clear shift in the peak of emission of CH_3OCHO and C_2H_5CN in 29 hot cores, over a sample of 60, while the other 28 sources show no shift in the position of the two molecules.

In these regions the origin of the observed chemical differentiation is still unclear. Caselli et al. (1993) proposed that the chemical differentiation between the Orion hot core and compact ridge could be related to differences in the thermal history of the sources. The use of time-dependent evaporation in chemical models by Viti & Williams (1999) and Viti et al. (2004), and later studies, such as Suzuki et al. (2018) and Garrod et al. (2022), confirmed that this chemical differentiation can be related to differences in the evolution of temperature within the sources. Thus, the presence of multiple young stellar objects embedded in high-mass star-forming regions, with different thermal history, could explain the chemical differentiation. Another possible explanation is the presence of accretion shocks at the centrifugal barrier around an accreting protostar, for example in the case of the source G328.2551-0.5321 (Csengeri et al. 2019). In summary, the suggested chemical differentiation between O- and N-bearing molecules does not have a clear explanation, and further studies are needed to fully understand the underlying processes.

The target of the G31.41+0.31 Unbiased ALMA sPectral Observational Survey (GUAPOS, Mininni et al. 2020; Colzi et al. 2021) is G31.41+0.31 (hereafter G31), a well-known and studied HMC located at a distance of 3.75 kpc (Immer et al. 2019) with a luminosity of $4.4 \times 10^4\,L_\odot$ and a gas mass $M \sim 70\,M_\odot$ (respectively from Osorio et al. 2009; Cesaroni 2019, after rescaling the value to the new distance estimate adopted). The core presents a velocity gradient observed in methyl cyanide and other COMs, such as methyl formate, first observed by Cesaroni et al. (1994), associated with a rotating toroid (Beltrán et al. 2004, 2005, 2018; Girart et al. 2009; Cesaroni et al. 2010, 2011, 2017). Observations of molecular lines detected the presence of molecular outflows and infall in this source (Girart et al. 2009; Cesaroni et al. 2011; Mayen-Gijon et al. 2014; Beltrán et al. 2018), which is also associated with free–free sources at 0.7 and 1.3 cm (Cesaroni et al. 2010; Beltrán et al. 2021). Previous observations of this source have always revealed a single millimeter compact core, until observations by Beltrán et al. (2021) made with ALMA at 1.4 mm and 3.5 mm and with the Very Large Array (VLA) at 7 mm and 1.3 cm with a resolution of ∼0.″15, ∼0.″075, ∼0.″05, and ∼0.″07, respectively, revealed the presence of four separate cores, named sources A, B, C, and D with gas masses of 16 $M_\odot$, 15 $M_\odot$, 26 $M_\odot$, and 26 $M_\odot$, respectively. They all have a part of (and in two cases the predominant fraction of) the emission at wavelengths equal to or above 7 mm coming from free-free emission. The total mass of the four fragments is $83 \pm 19\,M_\odot$, consistent within the errors with the mass of 70 $M_\odot$ estimated by Cesaroni (2019). Further high angular resolution analysis (at ∼0.09″) revealed the presence of infall in all four cores and the presence of at least six outflows detected in SiO, suggesting that each of the four sources embedded in the main core drives a molecular outflow (Beltrán et al. 2022a). This reveals that the sources are all still accreting material. Moreover, complementary large-scale observation of N_2H^+ performed with the IRAM 30 m telescope by Beltrán et al. (2022b) show that the environment in which G31 formed is a typical hub-filament system resulting from a cloud-cloud collision.

Previous studies explored the chemical richness of this HMC (e.g., Beltrán et al. 2005, 2009; Fontani et al. 2007; Isokoski et al. 2013; Calcutt et al. 2014; Rivilla et al. 2017; Gorai et al. 2021; Colzi et al. 2021; García de la Concepción et al. 2022), revealing the presence of several O-bearing and N-bearing COMs. Mininni et al. (2020) presented the GUAPOS project, aimed at studying

Table 1. Molecular species discussed in this work.

O-bearing species					
CH_3OH	$^{13}CH_3OH$	$CH_3^{18}OH$	CH_3CHO	$CH_3OCHO^{(a)}$	$CH_3COOH^{(a)}$
$CH_2OHCHO^{(a)}$	CH_3OCH_3	CH_3COCH_3	C_2H_5OH	aGg′-$(CH_2OH)_2$	gGg′-$(CH_2OH)_2$
N-bearing species					
CH_3CN	$^{13}CH_3CN$	$CH_3^{13}CN$	C_2H_3CN	C_2H_5CN	$C_2H_5^{13}CN$
O- and N-bearing species					
$CH_3NCO^{(b)}$	$NH_2CHO^{(b)}$	$CH_3C(O)NH_2^{(b)}$	$CH_3NHCHO^{(b)}$		

Notes. $^{(a)}$ Molecular species previously analyzed by Mininni et al. (2020); $^{(b)}$ molecular species previously analyzed by Colzi et al. (2021).

the full ∼32 GHz bandwidth spectrum at 3 mm, namely the whole Atacama Large Millimeter/submillimeter Array (ALMA) Band 3. The preliminary line identification revealed an extremely chemically rich source, with the spectrum showing only a few channels free of molecular line emission. Thus, G31 is an ideal candidate to investigate the complex chemistry in high-mass star-forming regions outside the Galactic center (GC), because the extreme conditions in the GC, in terms of interstellar radiation field and cosmic-rays flux can have an impact on the chemistry (see, e.g., Bonfand et al. 2019 and references therein). Most of the line emission in G31 arises from COMs, including both O-bearing and N-bearing species. Therefore, we aim to characterize the emission of these COMs in G31 and to investigate whether spatial segregation between N-bearing and O-bearing species is also present in this source. A first attempt to search for chemical segregation in G31, together with other five HMCs, was done by Fontani et al. (2007), who found a velocity difference of ∼0.6 km s^{-1} in the peak velocity of C_2H_5CN and CH_3OCH_3, with observations taken with the IRAM 30m telescope.

In this paper we analyze the emission of the following COMs: methanol, CH_3OH, and its isotopologs $^{13}CH_3OH$ and $CH_3^{18}OH$; acetaldehyde, CH_3CHO; dimethyl ether, CH_3OCH_3; acetone, CH_3COCH_3; ethanol, C_2H_5OH; ethylene glycol, aGg′-$(CH_2OH)_2$ and gGg′-$(CH_2OH)_2$ conformers; methyl cyanide, CH_3CN, and its isotopologs $^{13}CH_3CN$ and $CH_3^{13}CN$; vinyl cyanide, C_2H_3CN; and ethyl cyanide, C_2H_5CN, and its isotopolog $C_2H_5^{13}CN$. Moreover, in the discussion we consider the results from the analysis presented in this paper together with the results from the analysis of the three isomers of $C_2H_4O_2$ by Mininni et al. (2020), and of the O- and N-bearing COMs formamide, NH_2CHO; methyl isocyanate, CH_3NCO; acetamide, $CH_3C(O)CH_2$; and N-methylformamide, CH_3NHCHO, by Colzi et al. (2021) (see Table 1). In this work molecules including both O and N atoms will be considered as a separate class in the discussion, unlike other works in the literature where these molecules are considered among the N-bearing species. This choice allows us, in the case of observed spatial segregation in G31, to better investigate the behavior of these species and to study whether their emission is spatially closer to that of O-bearing species or N-bearing species.

In Sect. 2 we present the observations; in Sect. 3 we present the spectral analysis (Sect. 3.1) and the analysis of the maps (Sect. 3.2); in Sect. 4 we discuss the results of both the analysis of the spectrum and of the maps, to reveal the possible presence of chemical differentiation between N-bearing and O-bearing species or between selected molecular species. We also compare the abundances of COMs in G31 with other high-mass and low-mass star-forming regions, shocked regions, and quiescent clouds, and with chemical models. In Sect. 5, we summarize our main conclusions.

2. Observations

The observations were carried out with ALMA during Cycle 5, (project 2017.1.00501.S, P.I.: M. T. Beltrán), and cover the complete spectral range of ALMA band 3, between 84.05 GHz and 115.91 GHz (∼32 GHz bandwidth), with a spectral resolution of ∼0.488 MHz (∼1.3–1.7 km s^{-1}). The observations were divided into nine correlator configurations, and for each of them four contiguous basebands were observed. The data were first presented by Mininni et al. (2020), where it is possible to find more details about the spectral setups, the flux and phase calibrators, and the configurations of the correlators. The uncertainties in the flux calibration are ∼5% (from Quality Assesment 2 reports), in good agreement with ALMA Band 3 flux uncertainties reported by Bonato et al. (2018).

The data were calibrated and imaged with the Common Astronomy Software Applications package[1] (CASA; McMullin et al. 2007). The maps were created using a robust parameter of Briggs (1995) set equal to 0 and a common restoring synthesized beam of 1.″2 × 1.″2. The noise of the maps, rms, varies between 0.5 mJy beam^{-1} and 1.9 mJy beam^{-1}.

For all the observed basebands, the spectra were extracted from an area equal to the size of the beam and centered toward the peak of the continuum. Mininni et al. (2020) described the steps taken to align the spectra of the different correlator configurations and basebands to obtain the final spectrum. The baseline was analyzed by Colzi et al. (2021) with the software STATCONT (Sánchez-Monge et al. 2018) to statistically determine the value of the continuum level and then subtract it from the spectrum.

Both from the alignment of the different spectra and from the statistical analysis performed with STATCONT on the final spectrum, the uncertainty on the determination of the continuum level is ∼11%.

3. Analysis

3.1. Spectral fitting

The baseline-subtracted spectrum was analyzed with the Spectral Line Identification and Modeling (SLIM) tool within the MADCUBA package[2] (Martín et al. 2019). The spectroscopic data were taken from the Cologne Database for Molecular Spectroscopy[3] (CDMS, Müller et al. 2001, 2005) and from the JPL

[1] https://casa.nrao.edu

[2] Madrid Data Cube Analysis (MADCUBA) is a software package developed at the Center of Astrobiology (Madrid) to visualize and analyze data cubes and single spectra: https://cab.inta-csic.es/madcuba/

[3] https://cdms.astro.uni-koeln.de

database of molecular spectroscopy[4] (Pickett et al. 1998). Precise reference papers for each molecule analyzed in this work are given in Appendix A. For all the molecular species, except C_2H_5CN and its isotopologs, and C_2H_5OH, the partition function from the chosen catalog was either calculated using also the first excited states or their contribution was estimated to be less than 3% at temperatures below 300 K. For C_2H_5CN and its isotopologs the correction factor to the partition function is given in CDMS[5] and is above 3% from 75 K. Therefore, for C_2H_5CN and $C_2H_5^{13}CN$ we apply the correction factor (interpolated at the T resulting from the fit) to the column density obtained with MADCUBA. In the case of C_2H_5OH the partition function was calculated in CDMS (and also in JPL) taking into account the ground vibrational states only, but correction factors for temperatures different than 150 K (correction factor of 1.24 Müller et al. 2016) are not available yet. We calculated the correction factor at the temperature for this species in G31 (119 K, see Sect. 3.1.1) using the values of vibrational states energy by Durig et al. (2011).

The analysis was performed after a preliminary line identification, where we identified a large fraction of the molecular species present in the source (see Appendix E of Colzi et al. 2021). This line identification allowed us to check the presence of possible blendings of the transitions of the molecular species analyzed in this work with other species, and thus to select the most unblended transitions for each species to be used to constrain the fit.

To obtain the physical parameters of the molecular emission (column density N, excitation temperature T_{ex}, full width at half maximum FWHM, and velocity V_{LSR}) from the data, we assumed a single temperature component that fills the beam and used the AUTOFIT tool of MADCUBA-SLIM, which finds the best agreement, minimizing the χ^2, between the observed spectra and the predicted LTE model, also taking into account the optical depth. The simultaneous fit of multiple transitions for each molecular species allows the determination of V_{LSR} with an error smaller than the resolution in velocity of the spectrum ($\sim$1.5 km s^{-1}). During the fit we assumed local thermodynamic equilibrium (LTE), justified by the high density of G31 (rough estimate of $n \sim 10^8$ cm^{-3}, Mininni et al. 2020). The molecular species analyzed in this work are listed in Table 1.

The emission of methanol, methyl cyanide, and ethyl cyanide is optically thick, especially for the first two species, and thus we analyzed their isotopologs with ^{13}C and for CH_3OH and CH_3CN, even the transitions of the torsionally or vibrationally excited state (as already done in Colzi et al. 2021). To obtain the column density of the species containing only ^{12}C (i.e., the most abundant isotopologs) we multiplied the column density derived from the analysis of the ^{13}C isotopologs for the $^{12}C/^{13}C$ ratio. We adopted a value of $^{12}C/^{13}C = 37 \pm 12$, derived from Yan et al. (2019), and of $^{16}O/^{18}O = 333 \pm 143$, derived from Wilson & Rood (1994), using the galactocentric distance of 5.02 kpc for G31.[6]

For all the species we assumed an error of 11% on the values of N and T_{ex} to reflect the uncertainty on the level of continuum. The best LTE fit results are listed in Table 2. For the species in which the fit of the spectra was performed in previous GUAPOS papers (see Table 1, Mininni et al. 2020; Colzi et al. 2021) the results are listed in Table 3. The abundances were calculated using the column density of H_2 derived in the first paper of the GUAPOS project, $N_{H_2} = (1.0 \pm 0.2) \times 10^{25}$ cm^{-2} (Mininni et al. 2020).

From the spectral analysis it is already possible to infer preliminary hints of chemical differentiation. These are given by a clear difference in V_{LSR}, FWHM, or T_{ex} between O-bearing species, N-bearing species, and O- and N-bearing species or between selected molecular species. A difference in V_{LSR} would be the strongest indication since different embedded sources, resolved with observations at angular resolution of $\sim$0.″075 by Beltrán et al. (2021), would likely have slightly different velocities, while the values of FWHM or T_{ex} could be affected not only by a different position of the peak of the emission, but also by a different size of the emission. Figure 1 shows the mean maps of the emission of the different molecular species (see Sect. 3.2 for more details), where we can see that different species have different emission sizes.

The parameters derived from the best fit are given in Table 2, where instead of the absolute value of V_{LSR}, we give the difference $V - V_0$ using as reference velocity $V_0 = 96.5$ km s^{-1} (Beltrán et al. 2018).

3.1.1. O-bearing species

Methanol: CH_3OH, $^{13}CH_3OH$, and $CH_3^{18}OH$. We were not able to constrain the fit of CH_3OH $v = 0$ with a single temperature component. This could be connected both to the presence of a temperature gradient in the source, studied with high angular resolution data by Beltrán et al. (2018), and to the high abundance of this molecular species that leads to optically thick transitions. In Fig. B.1, we show some of the brightest transitions and we can see that some of them, which correspond to those having the lowest energies of the lower level and the highest Einstein coefficients, show inverse P Cygni profiles. Taking into account that the maximum recoverable scale of the GUAPOS project is $\sim$11″, it is unlikely that the filtering effect has a major impact. Therefore, we conclude that the inverse P Cygni profiles observed are due to the high optical depths of the lines and the presence of infall in the core, as reported by Beltrán et al. (2018, 2022a).

We analyzed the emission of the rotational transitions in the first torsionally excited state, $v_t = 1$, whose transitions have optical depths estimated by MADCUBA between 0.1 and 0.2, with only two exceptions. We constrained the fit using the seven unblended transitions available (see Table C.1). Both the observed spectrum and the synthetic spectrum from the best fit are given in Fig. B.2. The best-fit parameters are given in Table 2. These parameters are consistent with those found by the best visual agreement of the simulated spectrum with the transitions of CH_3OH in the ground state (Fig. B.1), with the exception of the column density which is a factor of $\sim$2 higher.

We also analyzed the emission of $^{13}CH_3OH$ and $CH_3^{18}OH$, whose lines are optically thin. The 12 unblended transitions used to constrain the fit of $^{13}CH_3OH$ are given in Table C.2, and the result of the fit is given in Table 2. The 12 transitions cover a broad range in E_U (energy of the upper state), from $\sim$7 K to $\sim$330 K. The spectrum of the transitions used to constrain the fit and the synthetic spectrum obtained with the best-fit parameters are given in Fig. B.3. The column density for CH_3OH derived multiplying the column density from the fit of $^{13}CH_3OH$ for the ratio $^{12}C/^{13}C = 37$ is $(3.6 \pm 0.7) \times 10^{19}$cm^{-2}.

For $CH_3^{18}OH$ we selected 15 transitions to constrain the fit (see Table C.3). These transitions cover a broad range in E_U from $\sim$5 K to $\sim$330 K. The spectrum of the transitions used to

[4] https://spec.jpl.nasa.gov/

[5] https://cdms.astro.uni-koeln.de/classic/predictions/catalog/archive/EtCN/Qvib.txt

[6] Calculated from the heliocentric distance of 3.75 kpc (Immer et al. 2019).

Table 2. Results of the spectral analysis.

Species	T_{ex} (K)	N (10^{17} cm^{-2})	X (10^{-8})	FWHM (km s^{-1})	$V - V_0$ (km s^{-1})
		O-bearing species			
CH_3OH $v_t = 1$	208 ± 24	100 ± 12	100 ± 30	8.3 ± 0.4	0.94 ± 0.15
$^{13}CH_3OH$	152 ± 20	9.6 ± 1.7	10 ± 3	7.2 ± 0.3	1.09 ± 0.10
$CH_3^{18}OH$	153 ± 20	2.4 ± 0.4	2.4 ± 0.7	7.0[a]	1.28 ± 0.13
CH_3OH[b]		800 ± 130	800 ± 200		
CH_3CHO	82 ± 20	0.34 ± 0.16	0.34 ± 0.18	7.5[a]	0.45 ± 0.11
CH_3OCH_3	98 ± 11	8.1 ± 1.0	8 ± 2	7.0[a]	1.07 ± 0.06
CH_3COCH_3	170 ± 21	5.6 ± 1.3	5.6 ± 1.4	7.0[a]	0.84 ± 0.06
C_2H_5OH	119 ± 14	4.7 ± 0.6[c]	4.7 ± 1.2[c]	7.02 ± 0.09	1.00 ± 0.04
aGg′-$(CH_2OH)_2$	120[a]	1.45 ± 0.17	1.5 ± 0.4	7.2[a]	0.48 ± 0.06
gGg′-$(CH_2OH)_2$	120 ± 28	0.87 ± 0.19	0.9 ± 0.3	7.2[a]	1.0 ± 0.2
		N-bearing species			
CH_3CN $v_8 = 1$	197 ± 51	3.2 ± 0.9	3.2 ± 1.1	8.6 ± 0.3	0.68 ± 0.15
$^{13}CH_3CN$	111 ± 17	0.073 ± 0.011	0.073 ± 0.019	7.1 ± 0.2	0.95 ± 0.09
$CH_3^{13}CN$	54 ± 10	0.069 ± 0.011	0.069 ± 0.018	7.2 ± 0.5	0.97 ± 0.19
CH_3CN[d]		2.7 ± 0.4	2.7 ± 0.7		
C_2H_3CN	104 ± 17	0.21 ± 0.04	0.21 ± 0.06	9.7[a]	1.05 ± 0.15
C_2H_5CN	83 ± 10	0.56 ± 0.08[e]	0.56 ± 0.14[e]	7.94 ± 0.13	1.37 ± 0.06
$C_2H_5^{13}CN$	126 ± 37	0.042 ± 0.012[f]	0.042 ± 0.017[f]	6.0[a]	1.8 ± 0.3
C_2H_5CN[g]		1.6 ± 0.5	1.6 ± 0.7		

Notes. Excitation temperature, T_{ex}; column density, N; abundance with respect to H_2, X; FWHM; and velocity with respect to $V_0 = 96.5$ km s^{-1}, $V - V_0$. The abundances were calculated using $N_{H_2} = (1.0 \pm 0.2) \times 10^{25}$ cm^{-2} (Mininni et al. 2020); to calculate the corrected values of column densities and abundances of a species from the analysis of its ^{13}C or ^{18}O isotopolog, we used the ratios $^{12}C/^{13}C = 37 \pm 12$ (from Yan et al. 2019) and $^{16}O/^{18}O = 333 \pm 143$ (from Wilson & Rood 1994), considering the galactocentric distance of G31, $D_{GC} = 5.02$ kpc; [a] quantity kept fixed during the fitting; [b] corrected values for column density and abundance derived from the values of $CH_3^{18}OH$; [c] corrected for the partition function factor at 119 K of 1.13; [d] corrected values for column density and abundance derived from the values of $^{13}CH_3CN$ (the estimate using the $CH_3^{13}CN$ would give corrected $N = (2.6 \pm 0.4) \times 10^{17}$ cm^{-2} and $X = 2.6 \pm 0.7$); [e] corrected for the partition function factor at 83 K of 1.062; [f] corrected for the partition function factor at 126 K of 1.24; [g] corrected values for column density and abundance derived from the values of $C_2H_5^{13}CN$.

Table 3. Results from the spectral and map analysis for O-bearing and O- and N-bearing COMs analyzed in previous papers of the GUAPOS project.

Species	T_{ex} (K)	N (10^{17} cm^{-2})	X (10^{-8})	$FWHM$ (km s^{-1})	$V - V_0$ (km s^{-1})	RA (J2000) (18h 47m s)	Dec(J2000) (–01° 12′ ″)	Reference
			O-bearing species					
CH_3OCHO	221 ± 27	20 ± 4	20 ± 6	6.8[a]	1.1[a]	34.318	46.054	Mininni et al. (2020)
CH_3COOH	250 ± 50[b]	6.4 ± 2.1[b]	6.2 ± 1.9[b]	7.8[a]	0.0[a]	34.315	46.057	Mininni et al. (2020)
CH_2OHCHO	128 ± 17	0.5 ± 0.09	0.50 ± 0.14	8.8[a]	0.0[a]	34.309	46.094	Mininni et al. (2020)
			O- and N-bearing species					
CH_3NCO[c]	91 ± 37	1.2 ± 0.3	1.2 ± 0.4	7.15[a]	0.5[a]	34.313	46.054	Colzi et al. (2021)
NH_2CHO[d]	150[a]	1.7 ± 0.6	1.7 ± 0.7	8.6[a]	0.5[a]	34.316	46.062	Colzi et al. (2021)
$CH_3C(O)NH_2$	285 ± 50	0.8 ± 0.4	0.8 ± 0.4	6.2 ± 0.4	0.2[a]	34.310	46.044	Colzi et al. (2021)
CH_3NHCHO	285[a]	0.37 ± 0.16	0.37 ± 0.17	7.0[a]	0.0[a]	34.307	46.058	Colzi et al. (2021)

Notes. The coordinates of the center of the emission of each species are derived from the task *imfit* applied to the mean maps. [a] Quantity kept fixed during the fitting procedure; [b] for CH_3COOH Mininni et al. (2020) found that the values of T_{ex}, N, and X were in the range 200–299 K, 4.3–8.4 × 10^{17} cm^{-2}, and 4.3–8 × 10^{-8}, respectively. The values reported in this table are the mean values of the ranges, while the errors cover the entire ranges. [c] From CH_3NCO $v_b = 1$; [d] from $NH_2^{13}CHO$, where the column density was multiplied by the factor $^{12}C/^{13}C = 37$.

constrain the fit and the synthetic spectrum obtained with the best-fit parameters are given in Fig. B.4, while the results of the fit are given in Table 2. The column density for CH_3OH derived multiplying the column density from the fit of $CH_3^{18}OH$ for the ratio $^{16}O/^{18}O = 333$ is $(8.0 \pm 1.3) \times 10^{19}$cm^{-2}.

The estimate of the column density of CH_3OH vt = 1 is a factor of 4 and 8 lower than that derived for CH_3OH from $^{13}CH_3OH$ and $CH_3^{18}OH$, respectively. This could be due to the different energy ranges covered by the transitions of the species: for CH_3OH vt=1 the available transitions all have $E_U/\kappa_B > 300$ K,

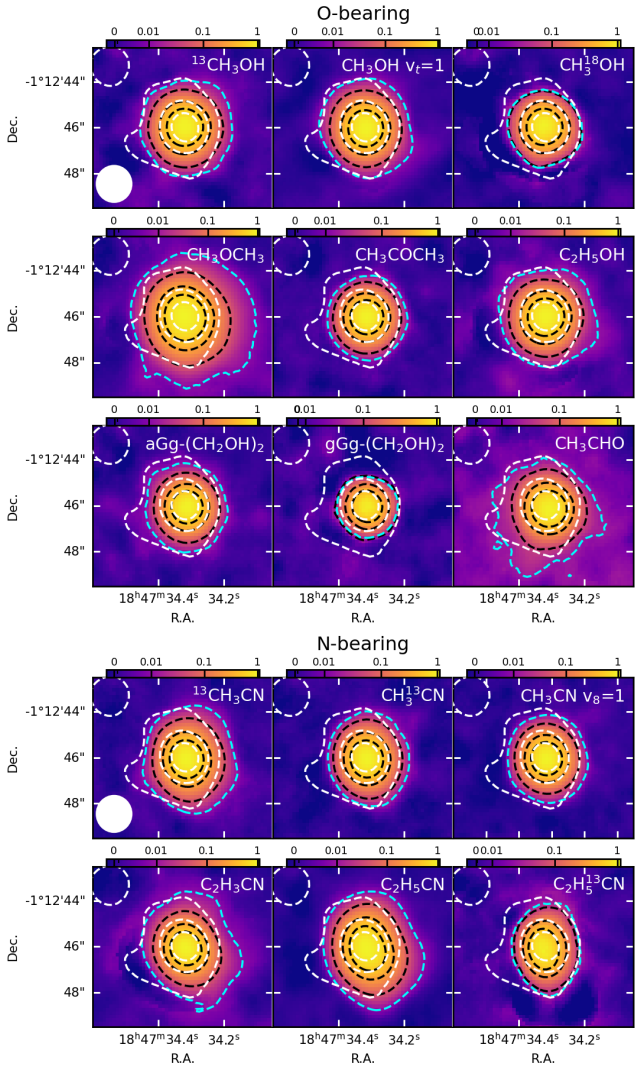

Fig. 1. Mean maps of the species for which the analysis is presented in this work for the first time (see Table 1). The mean maps were obtained by averaging the normalized maps of different transitions of the same species, and therefore they are in arbitrary units with peak close to unity. In dashed white lines are plotted the contour levels of the continuum map at 150, 60, and 20 times the value of rms = 0.8 mJy beam^{-1} (from Mininni et al. 2020). The black dashed lines delimit the contour where the intensity of the mean map drops to 50%, 25%, and 5% of the peak value. The 2D Gaussian fit ellipse to the emission is coincident with the inner black-dashed contour (50% level) for all the molecular species. The cyan dashed line delimits the contour where the intensity of the mean map is equal to 10 times the rms of the map. The size of the 1.″2 beam is indicated in the lower left corner of the first panel (top left).

while for the two isotopologs the transitions used to constrain the fit are in the range ∼5 –330 K. From the second-to-last column of Table C.2, and in Table C.3, we can see that $CH_3^{18}OH$ is optically thinner than $^{13}CH_3OH$. Therefore, in the discussion we adopt the value derived from $CH_3^{18}OH$ for the column density of CH_3OH since the two isotopologs give estimates of column density that differ by a factor of 2.

Acetaldehyde: CH_3CHO. We detected ten unblended lines of acetaldehyde. The spectral parameters of the corresponding transitions are given in Table C.4. The energy range of the upper level only covers energy transitions below 100 K (∼15–80 K). To help the fitting algorithm to converge, we fixed the FWHM to 7.5 km s^{-1}. This value was selected visually as the best value of FWHM to simulate the emission of individual transitions. The plot of the selected transitions with the superimposed synthetic spectrum calculated using the parameters from the best fit is given in Fig. B.5. The estimate of T_{ex} is lower than the mean value found for the rest of the molecular species, and could be due to the small range of E_U of the unblended transitions. To quantify how the column density would change if the temperature were higher, we performed a fit using the same transitions and fixing the value of T_{ex} to 120 K. The column density value from this fit is 6.0×10^{16} cm^{-2}, changing by a factor of ∼2 from the column density derived from the best fit.

Dimethyl ether: CH_3OCH_3. We identified 33 unblended transitions of dimethyl ether covering energies from ∼11 K to ∼230 K (see Table C.5). To help the fitting algorithm to converge, we fixed the FWHM to 7.0 km s^{-1}, the best value after a visual inspection. The results of the fit are given in Table 2. We found T_{ex} ∼ 100 K, only slightly lower than that of some other molecular species. However, this value of T_{ex} is likely real and not biased by the selected transitions used for the fit since in the fit we included several high-energy transitions. We plot the synthetic spectrum derived with the parameters of the best fit in Fig. B.6.

Acetone: CH_3COCH_3. We identified 38 unblended transitions of acetone, covering energies from ∼15 K to ∼170 K (see Table C.6). We report the best-fit parameters in Table 2. A small number of transitions of CH_3COCH_3 are overestimated by the best-fit model. A better agreement over the whole spectra would require a more accurate description of the temperature gradient of the source G31, as already seen for other molecular species (e.g., methanol; see Sect. 3.1.1.1). In Fig. B.7 we plot the most unblended transitions and the synthetic spectra obtained with the parameters of the fitting procedure.

Ethanol: C_2H_5OH. We detected 39 unblended transitions of ethanol. They are listed in Table C.7 and plotted in Fig. B.8. The energy of the upper level E_U covers a broad range, ∼17–350 K. The results of the best fit are given in Table 2, and the synthetic spectrum obtained using the parameters of the best fit is plotted in red over the observed spectrum in Fig. B.8. We note that the partition function from the catalog only considers the ground vibrational state, so we used the values of the energy of the vibrational states by Durig et al. (2011) to calculate the correction factor. For a temperature of 119 K the correction factor is 1.13, which we applied to correct the value of the column density.

Ethylene glycol: gGg′-$(CH_2OH)_2$ and aGg′-$(CH_2OH)_2$. We detected seven most unblended transitions of gGg′-$(CH_2OH)_2$, covering energies from ∼20 K to ∼120 K. They are listed in Table C.8 and plotted in Fig. B.9. To help the fitting algorithm to converge, we fixed the FWHM to 7.2 km s^{-1}. This value was selected visually evaluating the best value of FWHM simulating the emission of individual transitions. The results of the best fit are given in Table 2, and the synthetic spectrum obtained using the parameters of the best fit is plotted in red over the observed spectrum in Fig. B.9.

For the conformer aGg′-$(CH_2OH)_2$, already detected in G31 by Rivilla et al. (2017), we detected 20 unblended transitions. They are listed in Table C.9 and plotted in Fig. B.10. The energy of the upper level E_U covers an extremely narrow range between ∼15–55 K, with the exception of two transitions with E_U ∼ 100 K (at 85522.2 and 96259.9 MHz), which are blended with other transitions of lower energy of the same species. Therefore, to help the fitting algorithm to converge, we fixed the

excitation temperature to the value found for gGg′-$(CH_2OH)_2$ and the FWHM to 7.2 km , s^{-1}. The results of the best fit are given in Table 2, and the synthetic spectrum obtained using the parameters of the best fit is plotted in red over the observed spectrum in Fig. B.10. The ratio of the column density of the conformers aGg′/gGg′ is >1.

Isomers of $C_2H_4O_2$: CH_3OCHO, CH_3COOH, and CH_2OHCHO. The analysis of methyl formate, acetic acid, and glycolaldehyde is presented in Mininni et al. (2020). For CH_3OCHO, CH_3COOH, and CH_2OHCHO Mininni et al. (2020) selected the 22, 14, and 12 most unblended transitions, respectively, to perform the fit. These transitions covered a range in the energy of the upper level from ∼20 K to 220 K for CH_3OCHO, ∼20 K to 270 K for CH_3COOH, and ∼20 K to 190 K for CH_2OHCHO. The transitions were optically thin. The physical parameters derived from the spectral fitting are summarized in Table 3.

3.1.2. N-bearing species

Methyl cyanide: CH_3CN, $^{13}CH_3CN$, and $CH_3^{13}CN$. The transitions of CH_3CN v = 0 present within the observed GUAPOS bandwidth are $CH_3CN(5_K - 4_K)$ and $CH_3CN(6_K - 5_K)$. For CH_3CN v= 0, it was not possible to have a good convergence of the fit because the majority of the transitions (K = 0, 1, and 2) have high optical depths. The spectrum is plotted in Fig. B.11. We note that the lower K-components show a lower synthesized beam temperature than the higher K-components, a clear indication that the lower K-transitions are optically thick.

Because of the optical thickness of the ground transitions, we analyzed the vibrationally excited ones, CH_3CN v_8 = 1. The transitions used to constrain the fit are given in Table C.10. The results of the fit are given in Table 2, and the synthetic spectrum obtained with the best-fit parameters is given in Fig. B.12.

As for CH_3OH, we also analyzed the emission of the isotopolog $^{13}CH_3CN$. We detected only five transitions not affected by blending, with E_U between ∼10 K and ∼80 K. They are reported in Table C.11. The results of the best fit are given in Table 2 and plotted in Fig. B.13. Moreover, we analyzed the isotopolog $CH_3^{13}CN$. We detected only three unblended transitions, listed in Table C.12. The range in E_U is between ∼40 and ∼80 K. The results of the best fit are given in Table 2, and the spectrum is shown in Fig. B.14. The value of T_{ex} is lower than that of CH_3CN v_8 = 1 and $^{13}CH_3CN$. This discrepancy in T_{ex} could be due to the different (lower) energy range of the transitions used in the fit. Fixing the value of T_{ex} to 100 K the column density from the fitting procedure would be 8.1×10^{15} cm^{-2}, consistent inside the errors with the estimate leaving T_{ex} as a free parameter. From the second-to-last column of Table C.11 and C.12 we can see that $^{13}CH_3CN$ is optically thinner than $CH_3^{13}CN$, and therefore in the discussion we adopt the value derived from $^{13}CH_3CN$ for the column density of CH_3CN.

Vinyl cyanide: C_2H_3CN. We detected 11 unblended transitions of vinyl cyanide. They are listed in Table C.13 and plotted in Fig. B.15. The range in E_U is limited, between ∼30 and ∼90 K. To better constrain the fit, we fixed the value of the FWHM to 9.7 km s^{-1}. The results of the best fit (see Table 2) show a low value of T_{ex}. Such a low value could be a consequence of the low energy of the unblended transitions used for the fit.

Ethyl cyanide: C_2H_5CN and $C_2H_5^{13}CN$. We detected 16 unblended transitions of C_2H_5CN, listed in Table C.14. The E_U ranges from ∼25 to ∼120 K. The best-fit parameters are given in Table 2 and the associated synthetic spectrum is shown in Fig. B.16. The column density given in Table 2 was multiplied by the correction factor of the partition function at 83 K, which is 1.062. For C_2H_5CN the low value of T_{ex} could be a consequence of the low energy of the unblended transitions used for the fit. From Table C.14, we can see that some transitions have optical depths very close to unity, and in two cases above it. Therefore, the emission from this species is not optically thin, and we decided to analyze its isotopolog $C_2H_5^{13}CN$ as well to have a better estimate of its column density and abundance.

We detected only seven most unblended transitions of $C_2H_5^{13}CN$ (see Table C.15). The E_U ranges from ∼30 to ∼110 K. The intensity of the lines is weak, if the intensity of the other COMs is considered. The best-fit parameters are given in Table 2 and the associated synthetic spectrum is shown in Fig. B.17. The column density given in Table 2 was multiplied by the correction factor of the partition function at 126 K, which is 1.24.

3.1.3. O- and N-bearing species

The COMs formamide, NH_2CHO; methyl isocyanate, CH_3NCO; acetamide, $CH_3C(O)NH_2$; and N-methylformamide, CH_3NHCHO were analyzed by Colzi et al. (2021). The physical parameters derived from the spectral fitting are summarized in Table 3. NH_2CHO was detected in the ground vibrational state and in the first vibrational state. Moreover, $NH_2^{13}CHO$ was detected and analyzed. The values listed in Table 3 refer to the analysis of $NH_2^{13}CHO$, whose emission is more optically thin, where the column density had been corrected for a factor $^{12}C/^{13}C = 37 \pm 12$. For CH_3NCO, the ground vibrational state and the first vibrational state were detected and analyzed, with $^{13}CH_3NCO$ tentatively detected because most of the transitions are contaminated or blended with transitions of other species. The values listed in Table 3 are derived from the analysis of the first vibrational state. $CH_3C(O)NH_2$ ground state and excited states (v_t = 1, 2) had optical depths ≪1, and were fitted together. For its isomer CH_3NHCHO, only transitions of the ground state were detected, and to perform the fit the temperature was fixed to the value derived for $CH_3C(O)NH_2$.

3.2. Analysis of the maps

To create the emission maps of the species analyzed in this work we selected for each of them eight of the most unblended lines,[7] or the greatest number possible for those species for which we detect fewer than eight (mostly) unblended transitions to fit. We selected the lines for the maps among the range of the detected unblended transitions to include both low and high upper state energy transitions E_U. The transitions corresponding to the selected lines are indicated in the last column of Tables C.1−C.15. To create the maps of each line, we first removed the continuum emission from the cubes using the software STATCONT (Sánchez-Monge et al. 2018), and then created the integrated intensity (moment-0) map for each line.

To obtain a mean map of each species, we normalized each map to its peak intensity and then averaged all the maps of the same species together, using the task *immath* of CASA. Normalizing the different maps before averaging allows us to give the

[7] What here is called a *line* can be the result of the emission of multiple transitions of the same species, whose frequencies are closer than FWHM/2. Therefore, eight lines do not necessarily correspond to only eight transitions.

Table 4. Results of the 2D Gaussian fit to the mean maps.

Species	E_U/k_B (K)	RA(J2000) (18h 47m s)	Dec (J2000) (–01° 12′ ″)	$\theta_{max} \times \theta_{min}$ (″ × ″)	P.A. (deg)
O-bearing species					
$CH_3OH\ v_t = 1$	~300–800	34.317	46.035	1.61 × 1.58	34
$^{13}CH_3OH$	~10–330	34.319	45.990	1.66 × 1.62	88
$CH_3^{18}OH$	~10–330	34.323	45.972	1.62 × 1.57	75
CH_3CHO	~10–70	34.308	46.132	1.64 × 1.60	50
CH_3OCH_3	~10–220	34.319	46.052	1.98 × 1.83	22
CH_3COCH_3	~10–170	34.314	46.026	1.51 × 1.49	80
C_2H_5OH	~10–280	34.318	46.018	1.67 × 1.62	113
$aGg'\text{-}(CH_2OH)_2$	~15–55	34.312	46.068	1.46 × 1.44	57
$gGg'\text{-}(CH_2OH)_2$	~25–115	34.313	46.035	1.42 × 1.38	66
N-bearing species					
$CH_3CN\ v_8 = 1$	~530–590	34.316	46.047	1.47 × 1.43	24
$^{13}CH_3CN$	~10–80	34.313	46.069	1.71 × 1.57	16
$CH_3^{13}CN$	~40–80	34.314	46.056	1.64 × 1.51	14
C_2H_3CN	~20–80	34.316	46.084	1.57 × 1.41	35
C_2H_5CN	~20–120	34.311	46.094	1.95 × 1.59	20
$C_2H_5^{13}CN$	~20–100	34.322	46.105	1.77 × 1.41	7

Notes. Results of the 2D Gaussian fit only for the species for which the analysis is presented in this work for the first time (see Table 1), performed with the task *imfit*. In the second column we give the range in upper state energy E_u of the transitions used to create the mean maps.

same weight to every map, and to obtain a mean map in which the FWHM of the emitting region is not biased by the brightest lines.

The mean maps obtained with this procedure are shown in Fig. 1, and were fitted with a 2D Gaussian using the task *imfit* inside CASA to obtain the position of the peak of emission and the size of the emission. The results of the 2D Gaussian fit are given in Table 4 for the molecular species analyzed in this paper. The maps of the emission of the three isomers of $C_2H_4O_2$ and of O- and N-bearing species were already presented in Mininni et al. (2020) and Colzi et al. (2021) and are not shown in this paper, while we report the position of the center of emission in Table 3. The coordinates of the peak of the emission for CH_3NCO, NH_2CHO, $CH_3C(O)NH_2$, and CH_3NHCHO were derived from the maps presented in Colzi et al. (2021) following the same methodology presented in this paper and in Mininni et al. (2020).

The task *imfit* also produces the maps of the residuals (i.e., the difference between the maps in input and the best 2D models computed by the task itself), where it is possible to understand if there is some molecular emission not coming from the main core (modeled with the 2D Gaussian), but from more extended regions or from secondary spots in the map. The maps of the residuals are plotted in Fig. 2.

4. Discussion

4.1. Emission morphology

From the mean maps of the different species shown in Fig. 1, we can see that the emission of all the COMs analyzed is centered toward the continuum peak of the HMC, with some species showing a shape not perfectly Gaussian. Among the O-bearing species, we can see that the contours of the emission of CH_3CHO are shifted toward the southwest direction when compared to the contours of the continuum, unlike all the other O-bearing species ($aGg'\text{-}(CH_2OH)_2$ shows a less significant shift in the same direction). Looking at the residual maps in Fig. 2 (which shows a region about two times larger around G31 with respect to Fig. 1), we can see that CH_3CHO, CH_3OCH_3, $^{13}CH_3CN$, C_2H_3CN, and C_2H_5CN show a residual emission over ten times the rms value (cyan contours). In all cases, this emission is concentrated on the west and southwest edge of the main core (excluding residuals in the center of the core), with the exception of CH_3CHO, which shows very diffuse emission in all the envelope around the HMC, with spots over the 10 rms level, and a prominent more compact spot at the southern edge of the G31 main core. The origin of the residual emission could be related to the presence of outflows in the east–west direction and southwest–northeast direction on the plane of the sky, like those mapped in SiO by Beltrán et al. (2018, 2022a). The more extended morphology of CH_3CHO cannot be explained only by the fact that we cover a lower energy transition, even if the extended emission is more prominent in the lower energy state moment maps of CH_3CHO among those used to create the mean-moment map. In Appendix D, we show the moment-0 maps of a low-energy transition for each molecular species, and none of the other moment-0 maps shows such an extended emission, even in the low-energy transitions.

All these regions are located outside the 1.″2 central region from which we extracted the spectrum. It should be noted that the brightness peak of this residual emission is two orders of magnitude below the brightness toward the main core (which is 1 in the units of Figs. 1 and 2, from the methodology used to obtain the mean maps described in Sect. 3.2), and thus the column densities in those regions are expected to be accordingly smaller than those derived toward the center of the G31 HMC.

4.2. Positions of molecular species emission peaks

To reveal the existence of chemical differentiation inside this source we calculated the position of the peak of the emission for each molecular species, as described in Sect. 3.2.

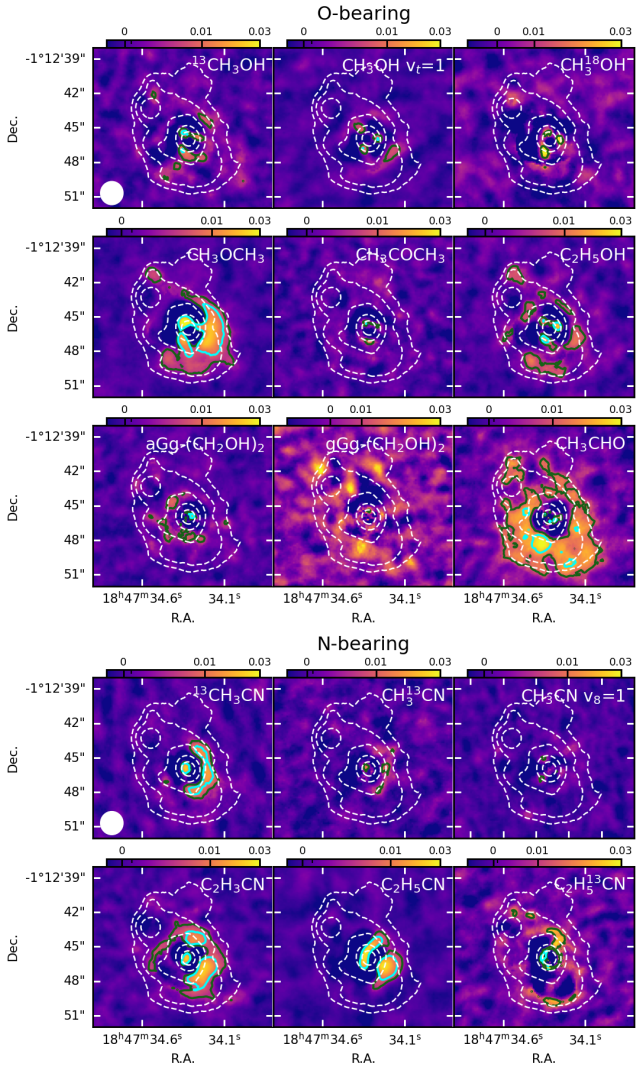

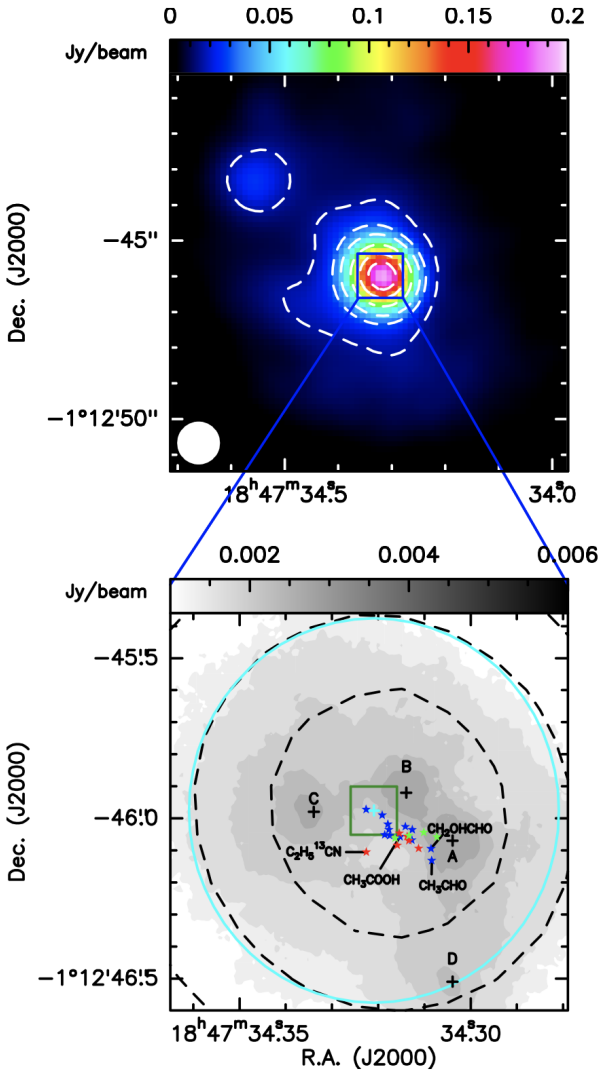

Fig. 2. Maps of residuals after the 2D Gaussian fit to the mean maps for the species for which the analysis is presented in this work for the first time (see Table 1). The size of the plotted region is larger than that plotted in Fig. 1. The units are the arbitrary units of the mean maps. In white are plotted the contour levels of the continuum map at 150, 60, 20, 10, and 5 times the value of rms = 0.8 mJy beam^{-1} (from Mininni et al. 2020). The green and cyan solid lines delimit the contours of the regions where the emission in the residual map is larger than 5 and 10 times the rms, respectively. The size of the 1.″2 beam is indicated in the lower left corner of the top left panel.

Fig. 3. Position of molecular emission peak over continuum map of G31. Upper panel: Continuum map from Mininni et al. (2020). The beam of 1.″2 of the GUAPOS data is given in the lower left corner. The contour levels are at 20, 40, 60, 100, 150, and 200 times the value of rms = 0.8 mJy beam^{-1}. Lower panel: Zoomed-in image of upper panel, where the black dashed contours are the two inner contours (150 and 200 times the rms) of the continuum image from the GUAPOS data at a resolution of 1.″2, while the grayscale map (0.08, 0.12, 0.2, 0.4 mJy beam^{-1}) is the continuum map at 3.5 mm from Beltrán et al. (2021) with an angular resolution of ∼0.″075. The dimension of the beam is given in the lower left corner, while the 1.″2 beam of the GUAPOS data is shown as the cyan circular contour. The four black crosses give the positions of the four compact sources detected by Beltrán et al. (2021), and the green square indicates the dimension of the pixel in the GUAPOS maps and cubes, centered around the position of the peak of the GUAPOS continuum, indicated by the cyan cross. The blue stars indicate the positions of the peak of the emission of O-bearing species, red stars indicate the positions of the peak of the emission of N-bearing species, and green stars indicate the positions of the peak of the emission of O- and N-bearing species. The errors of the positions of the peak of molecular species are comparable to or below the dimension of the star symbols.

The coordinates are reported in Table 4 for the molecular species analyzed in this work, and in Table 3 for the molecular species presented in Mininni et al. (2020) and Colzi et al. (2021).

The distances between the center of emission of the different species are smaller than the beam (1.″2); therefore, the spatial resolution of the observations is not sufficient to have conclusive results about the possible presence of spatial segregation for some classes of molecular species or for selected species.

Nevertheless, to give a visual reference to be confirmed by higher angular resolution data, in Fig. 3 we plot the continuum emission of the GUAPOS data and the high-resolution continuum data at 3.5 mm from Beltrán et al. (2021). The blue stars give the position of the peaks of the emission of O-bearing COMs, red stars the peak positions of N-bearing COMs, and green stars the peak positions of O- and N-bearing COMs. The error bars on the peak position given in the output of the 2D Gaussian fit performed with the *imfit* tool of CASA are below the dimension of the maps pixel for all the molecular species. This is due to the fact that the emission is nearly Gaussian, with the residual values contributing at most a factor of 3% with respect to the peak emission. These error bars were

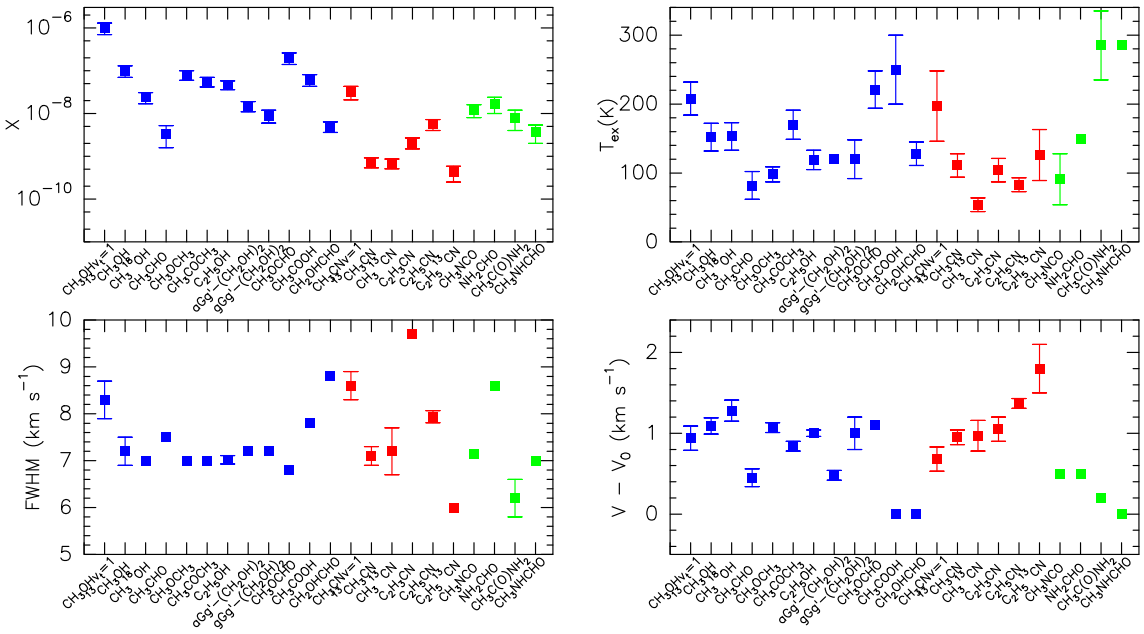

Fig. 4. Abundance X, excitation temperature T_{ex}, full width at half maximum FWHM, and line velocity $V - V_0$. Shown in blue are the O-bearing species, in red the N-bearing species, and in green the O- and N-bearing species.

not plotted in the bottom panel of Fig. 3 because they are of the same dimension as the star-shaped symbols used for the peak positions. The highest spatial separation is found among the majority of O-bearing molecules and the position of the peak of CH_3CHO and CH_2OHCHO. In the previous section we also highlighted a shift of the contour of emission of CH_3CHO with respect to the emission of the other O-bearing COMs. Only one molecular species, $C_2H_5^{13}CN$, is located far away from the position of any of the cores.

4.3. Spectral analysis

The abundances with respect to H_2 of the COMs analyzed in G31 range from $\sim 10^{-6}$ (CH_3OH) to $\sim 10^{-10}$ ($C_2H_5^{13}CN$). In the case of methanol, the estimate for the column density derived from the $v_t = 1$ state is a factor of 4 lower than the estimate obtained from the ^{13}C isotopolog, rescaled with the factor $^{12}C/^{13}C$, indicating that the fit of the torsionally excited state might still be affected by an optical depth effect. On the contrary, the estimates for the column density and abundance of CH_3CN from the $v_8 = 1$ state and from its two ^{13}C isotopologs are consistent within the errors, despite the large differences in T_{ex} derived for the three species. The estimate for ethyl cyanide from the ^{13}C isotopolog is a factor of 2 larger than the estimate from the emission of the main isotopolog, whose transitions have optical depths close to 1 (see Table C.14). Figure 4 shows the comparison among the physical parameters of the molecular species presented in this work, together with CH_3OCHO, CH_3COOH, CH_2OHCHO, CH_3NCO, NH_2CHO, $CH_3C(O)NH_2$, and CH_3NHCHO from Mininni et al. (2020) and Colzi et al. (2021). We summarize the data for these molecular species in Table 3.

As discussed in Sect. 3.1, the analysis of the physical parameters of the emitting gas derived from the spectral analysis of the COMs can give further hints on the presence of a chemical differentiation. The most robust hints are given by a difference in the peak velocity of different molecular species. Other authors have also reported clear differences in T_{ex} among O-bearing and N-bearing species (e.g., Bøgelund et al. 2019), but in G31 part of the discrepancy in T_{ex} might be due to the difference in size of the emitting regions of different species since there is clear evidence of a temperature gradient inside this HMC (Beltrán et al. 2005).

In Fig. 4, the value T_{ex} does not show a clear difference between O-bearing species, N-bearing species, and O- and N-bearing species. The values range from ∼60 K to ∼300 K depending on the molecular species. This broad range might be due to emission arising from different regions (see Table 4) or from the fact that some of the molecular species presented in this work do not have unblended transitions with $E_U > 100$ K, leading to possibly underestimated excitation temperatures.

The FWHM values vary between 6 and 10 km s^{-1}, not showing any particular trend among molecular species. On the contrary in $V - V_0$ we can see that the majority of the molecular species have $V - V_0$ close to 1 km s^{-1} (including $C_2H_5^{13}CN$ since its value is consistent with ∼1 km s^{-1} inside the large uncertainty), with the exception of CH_3CHO, CH_3COOH, CH_2OHCHO, aGg′-$(CH_2OH)_2$, and the four O- and N-bearing species CH_3NCO, NH_2CHO, $CH_3C(O)NH_2$, and CH_3NHCHO. In particular, CH_3COOH, CH_2OHCHO, $CH_3C(O)NH_2$, and CH_3NHCHO have $V - V_0 \sim 0.2$–0.0 km s^{-1}, while for CH_3CHO, CH_3NCO, aGg′-$(CH_2OH)_2$, and NH_2CHO the difference is less pronounced, with $V - V_0 \sim 0.5$ km s^{-1}. A previous study by Fontani et al. (2007) found a discrepancy of ∼0.6 km s^{-1} between the velocity of C_2H_5CN and CH_3OCH_3 in G31 from IRAM 30 m telescope data, while in the interferometric data at a resolution of 1″.2 presented in this paper the discrepancy is only ∼0.3 km s^{-1}.

From these results and the tentative analysis of the positions of the peak of the emission presented in the previous section, there are possible indications of chemical differentiation. The stronger indications are for CH_3CHO and CH_2OHCHO, which have the largest separation in the peak position from all the other O-bearing species, and a discrepancy also in $V - V_0$, while for CH_3COOH, aGg′-$(CH_2OH)_2$ and O- and N-bearing species we have a difference in peak velocity, but not a clear difference in peak position in our 1″.2 resolution maps.

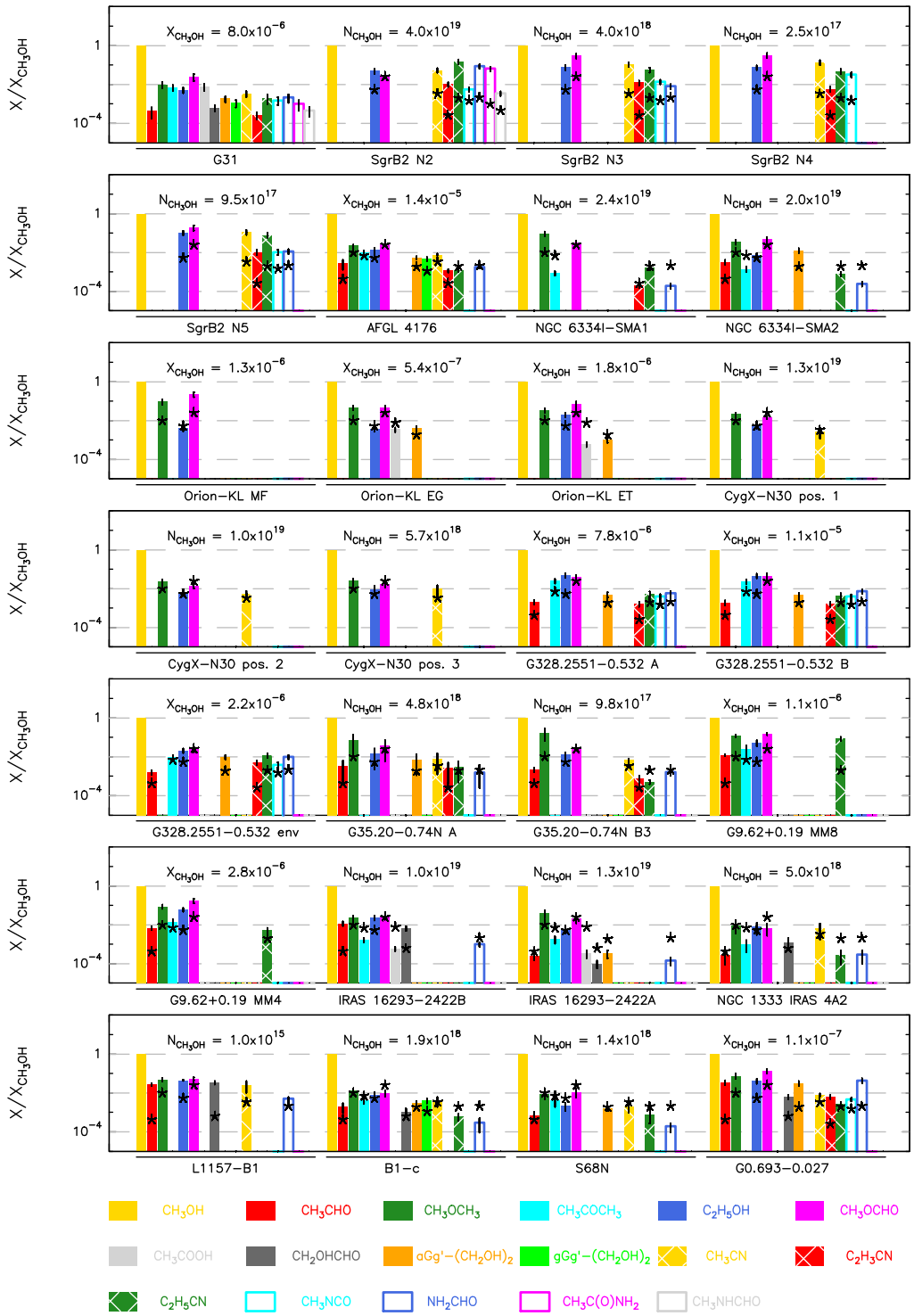

Fig. 5. Histograms of O-bearing, N-bearing, and O- and N-bearing COMs abundances with respect to methanol for G31 (this paper, Mininni et al. 2020, and Colzi et al. 2021); SgrB2-N2/N3/N4/N5; AFGL4176; NGC 6334I-SMA1 and SMA2 (from SMA data analysis); Orion-KL methyl formate peak (MF), ethylene glycol peak (EG), and ethanol peak (ET); CygX-N30 at the position 1, 2, and 3 as described in van der Walt et al. (2021); G328.2551-0.532 A, B, and inner-envelope position as in Csengeri et al. (2019); G35.20-0.74N A and B3; IRAS 16293-2422 A and B; NGC 1333 IRAS 4A2; L1157-B1; B1-c; S68N; and G+0.693-0.027. For the sources whose abundances were not available the ratio of column densities is plotted since $X/X_{CH_3OH} = N/N_{CH_3OH}$. In the upper part of each panel are reported the absolute values of X_{CH_3OH} (or N_{CH_3OH} in cm^{-2}, if the abundance is not available) for each source. To better compare the different sources with G31, the values of X/X_{CH_3OH} in G31 are flagged with asterisks above the histogram of all the other sources.

4.4. Comparison with other sources

In Fig. 5, we plot the abundances with respect to methanol of the O-bearing, N-bearing, and O- and N-bearing species detected in G31, together with the abundances of the same COMs found in other twenty-seven sources in literature. These include the HMCs SgrB2 N2/N3/N4/N5 (Belloche et al. 2016; Bonfand et al. 2019); AFGL4176 (Bøgelund et al. 2019); NGC 6334I- SMA1

and SMA2 (Zernickel et al. 2012); the Orion-KL observation toward the methyl formate peak (MF), ethylene glycol peak (EG), and ethanol peak (ET) of O-bearing molecules only (Tercero et al. 2018); the protostellar source CygX-N30 in position 1, 2, and 3 analyzed by van der Walt et al. (2021); G35.20-0.74N A and B3, the two most chemically rich sources in G35.20–0.74N analyzed by Allen et al. (2017); the two most chemically rich sources MM8 (HMC) and MM4 (late HMC or hyper compact HII region) in the source G9.62+0.19 (Peng et al. 2022); the low-mass hot corinos IRAS 16293-2422 A and B (Jørgensen et al. 2016, 2018; Coutens et al. 2016; Lykke et al. 2017; Manigand et al. 2020); NGC 1333 IRAS 4A2 (López-Sepulcre et al. 2017; Taquet et al. 2019); B1-c and S68N (van Gelder et al. 2020; Nazari et al. 2021); the positions of accretion shocks in high-mass star-forming regions G328.2551-0.532 A and B (Csengeri et al. 2019); the shocked region L1157-B1 associated with a low-mass young stellar object (YSO, Lefloch et al. 2017; Codella et al. 2009); the inner envelope position around a HMC precursor G328.2551-0.532-env (Csengeri et al. 2019); and the molecular cloud G+0.693-0.027 (Requena-Torres et al. 2006, 2008; Zeng et al. 2018; Bizzocchi et al. 2020; Rodríguez-Almeida et al. 2021; Rivilla et al. 2022; Sanz-Novo et al. 2022) located toward the northeast of the SgrB2 star-forming complex in the Central Molecular Zone (CMZ). Even though we are interested in discussing the relative abundances of these molecular species in different sources, in Fig. 5 we also report the absolute value of the abundance (or the column density if abundance was not available) of methanol in each source. For G+0.693-0.027 we rescaled all the abundances to the value of $N(H_2)$ derived by Martín et al. (2008), used in all the recent works toward this source.

Before comparing the abundances in G31 with the other HMCs, we checked for the presence of a possible beam-dilution effect in the column density and abundance estimates of G31, given that the beam of 1.″2 probes a linear scale of ∼4400 au, larger than the scale resolved in some of the other studies toward HMCs we included in the comparison. Colzi et al. (2021) presented the emission maps of O- and N-bearing species at a higher resolution of 0.″2, and confirmed that for these species the emission fills the beam of 1.″2 of the data analyzed in this paper. Moreover, the estimate of the column density from the high-resolution data is consistent within a factor of 2 with the estimate obtained with our resolution. We also compared the column density of CH_3OCHO derived from the data at 1.″2 with that obtained from the analysis of the data at 0.″2 presented by Beltrán et al. (2018), and they are in good agreement. Beltrán et al. (2018) also show the high-resolution map of the integrated emission of CH_3CN (12-11) K = 2, which covers the region of our 1.″2 beam. Therefore, we conclude that possible beam-dilution effects will be minor if present, and will not affect the discussion below.

Comparing the abundances found in G31 and in the other high-mass protostars, we found discrepancies: the four sources located toward the GC (SgrB2 N2/N3/N4/N5) show in general higher abundances, around one order of magnitude or more in most of the cases, of O-bearing species (only CH_3OCHO and C_2H_5OH) and especially of N-bearing species and O- and N-bearing species. This enrichment of COMs with respect to methanol toward the GC may be the result of the peculiar conditions found in those regions, such as the cosmic-ray ionization rate being a factor of ∼50 higher than the solar neighborhood value (Bøgelund et al. 2019), which can enhance the efficiency of some chemical pathways. For AFGL4176, we found a good general agreement of the abundances with those in G31, with some smaller differences for CH_3CHO, aGg′-$(CH_2OH)_2$, gGg′-$(CH_2OH)_2$, and C_2H_3CN. The absolute abundance of methanol with respect to H_2 in this source is higher by a factor of ∼4 than the value derived for G31. The abundances of CH_3OCH_3, CH_3COCH_3, and NH_2CHO toward NGC 6334I-SMA1 show clear discrepancies with the values in G31, while CH_3OCHO and C_2H_5CN abundances are in good agreement. In the case of NGC 6334I-SMA2, only half of the COMs selected have abundances comparable to those found in G31. The comparison with the three positions in Orion-KL is limited to only five O-bearing species: CH_3OCH_3, C_2H_5OH, CH_3OCHO, CH_3COOH, and aGg′-$(CH_2OH)_2$. The best agreement is found between G31 and the ethylene glycol peak (EG see Tercero et al. 2018). Also in the case of CygX-N30 (van der Walt et al. 2021) the comparison is limited to only four species: CH_3OCH_3, C_2H_5OH, CH_3OCHO, and CH_3CN. The abundances with respect to methanol of the three O-bearing species do not vary significantly toward the three positions identified by van der Walt et al. (2021) and are in good agreement with the values measured toward G31, while the abundance of CH_3CN presents more variability with position 1, having a value close to that of G31.

The abundances of C_2H_5OH, CH_3OCHO, CH_3CN, C_2H_5CN, and NH_2CHO in G35.20-0.74N A by Allen et al. (2017) are comparable with those in G31, while the other molecular species are in general more abundant than in G31. For G35.20-0.74N B3, the abundance of C_2H_3CN is similar to that of G31, while the abundance of C_2H_5CN is clearly lower. The rest of the molecular species have abundances with respect to methanol close to those found for G35.20–0.74N A. The abundances in cores MM8 and MM4 of G9.62+0.19 are in general higher than those found toward G31, in particular CH_3CHO in both sources and C_2H_5CN in MM8, which show a very high abundance with respect to methanol, similar to the values found toward the GC.

Overall, it seems that there is not a unique template for the abundances of COMs in HMCs. This could be the result of the peculiar physical properties (and their evolution with time) of each source, together with different environmental conditions that can affect the chemistry. The thermal history of each source has an impact on the reactions that can occur and on their efficiency, likely leading to different abundance values (Caselli et al. 1993; Viti & Williams 1999; Viti et al. 2004; Suzuki et al. 2018). As an example, in the chemical models by Garrod et al. (2022) the abundances of N-bearing molecules are more sensitive to the time evolution of the warm-up phase (see Sect. 4.5), while the O-bearing species are more representative of the low-temperature dust-grain chemistry. Thus, the different thermal evolution with time of each source can lead to different abundances with respect to H_2 of N-bearing and O-bearing species, and also of the abundances with respect to methanol. Moreover, other environmental factors, such as the cosmic-ray ionization rate and the different N/O elemental abundance in each particular region, have an impact on the chemistry.

In the case of hot corinos, the range of abundances with respect to methanol of the COMs is similar to the range of abundances found toward G31 and other HMCs. However, among the five sources (IRAS 16293–2422 A and B, NGC 1333 IRAS 4A2, B1-c, and S68N) only S68N shows an overall agreement with the majority of the COMs abundances estimated in G31, with the exception of NH_2CHO, which is one order of magnitude less abundant. In IRAS 16203–22422 B we have pairs of COMs that show inverted abundances compared with G31. These are CH_3CHO and CH_3COCH_3 together with the two isomers CH_3COOH and CH_2OHCHO. In IRAS 16203–22422 A, almost all the COMs show lower abundances with respect to methanol than in G31, except for CH_3OCH_3, while

for B1-c only half of the abundances are similar to those found toward G31.

The accretion-shock regions G328.2551–0.532 A and B display slightly higher abundances of almost all the COMs presented in Fig. 5 for comparison. This is also true for the shock position driven by a low-mass protostar, L1157-B1, where we have steeper increases of abundance for CH_3CHO and CH_2OCHO. The abundances in the envelope around a HMC precursor in G328-2551–0.532 also show, in general, higher values. Finally, we compare the abundances found in G31 with those toward G+0.693–0.027, a giant molecular cloud located inside the CMZ. The abundances of CH_3CHO, CH_2OHCHO, aGg′-$(CH_2OH)_2$, C_2H_3CN, and NH_2CHO with respect to CH_3OH are a factor of ∼10 or more higher than the abundances in G31, while the discrepancies with the other species are less pronounced. However, the value of column densities of CH_3OH is three orders of magnitude lower than in G31. The presence of these complex molecules in this source is thought to be the result of sputtering of dust grains and their icy mantles (e.g., Requena-Torres et al. 2006, 2008), together with the action of high cosmic-ray fluxes that enhances the efficiency of ion-neutral reactions increasing the abundances of some molecular species, since this source is located in the GC.

From these comparisons the chemical content of G31 in COMs is not comparable to that of sources in the GC due to the peculiar conditions found in those regions, and among other HMCs outside the central region of the galaxy we have a spread in chemical abundances among the sources. The only source with a remarkable similarity in chemical composition with G31, over the large number of molecules presented in this discussion, is AFGL4176. It is likely that the differences seen with respect to the other HMCs are due to the different thermal histories of the various sources. Moreover, abundances with respect to methanol in hot corinos are slightly lower than those found in G31 as general trend, with the exception of IRAS 16293–2422 B, which does not show overall similar ratios. On the other hand, the abundances with respect to methanol found toward shocked regions in high-mass and low-mass star-forming regions, show higher abundances than those of HMCs located outside the GC (e.g., G31).

4.5. Comparison with chemical models

In this section we compare the abundances of COMs in G31 with the results of the final models presented by Garrod et al. (2022). The work by Garrod et al. (2022) is one of the most comprehensive models of gas-grain chemistry to date, and it predicts the abundances of several molecular species in HMCs and hot corinos, including a large number of COMs. In particular, nondiffusive reaction mechanisms (Eley–Rideal mechanism, three-body reactions, three-body excited-formation reactions, and photodissociation-induced reaction mechanism) are implemented and the chemical network is updated with new routes proposed in recent years for the formation or destruction of dimethyl ether, formaldehyde, glycolaldehyde, and ethylene glycol (e.g., Balucani et al. 2015; Ayouz et al. 2019).

The model has two physical phases. The first phase is the cold free-fall collapse phase in which the gas temperature is fixed to 10 K, while density increases to $2 \times 10^8 cm^{-3}$ (consistent with the rough estimate given for G31 of $\sim 10^8\,cm^{-3}$ by Mininni et al. 2018). The second phase is the warm-up phase where the density is constant and the temperature increases up to 200 K on three different timescales for the three different models (slow timescale 5×10^4 yr, medium timescale 2×10^5 yr, and fast timescale 1×10^6 yr). All three models then continue until a temperature of 400 K is reached.

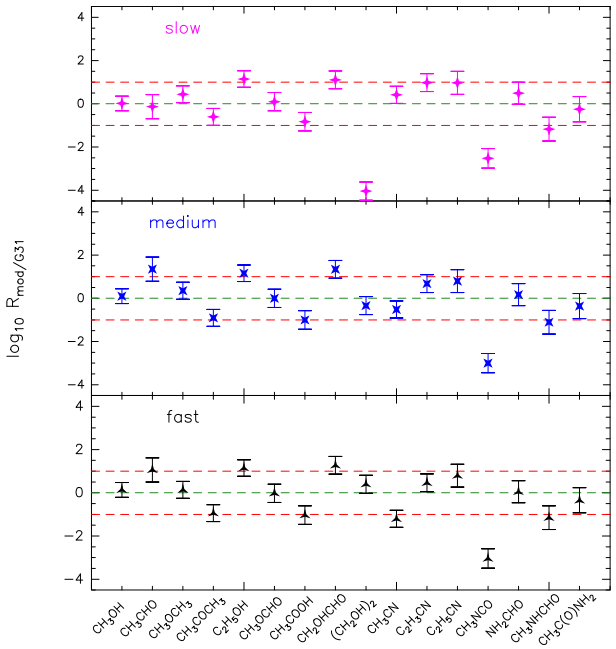

Fig. 6. Ratio of abundances from model by Garrod et al. (2022) to abundances derived for G31. The three panels use the abundances of the three different warm-up timescale chemical models. An error of 30% is considered on the values of the abundances from the chemical models. The green dashed line represents a ratio $R_{mod/G31} = 1$, while the two red dashed lines represent $R_{mod/G31} = 0.1$ and 10.

In Fig. 6, we plot the ratio of the peak abundances reached in the three final models (slow in the upper panel, medium in the middle panel, and fast in the lower panel) to the abundance derived in G31 for the COMs presented in this work. We assumed an error of 30% on the values derived from the chemical models. The agreement between the models and the abundances in G31 is remarkable, with only a few molecular species overabundant or underabundant in G31 by more than a factor of 10 with respect to the abundances derived by Garrod et al. (2022). The best overall agreement is with the slow model with a few exceptions, but the values from the medium model are also very close to those of G31. A large difference between these two models is seen in $(CH_2OH)_2$, for which the value found in G31 is in very good agreement ($R_{mod/G31} \sim 1$) with the prediction of the medium model, while it is 10^4 times overabundant compared with the slow model. In the latter model the destruction pathway of $(CH_2OH)_2$ on the dust grains via H abstraction has more time to act, leading to the low value presented in Fig. 6. This might indicate that the best match with G31 could be with an intermediate timescale between the slow and the medium values. The only species that is not well reproduced by any of the models is CH_3NCO, which is at least a factor of 500 more abundant in G31. This species is underproduced by the models also when compared with SgrB2(N2) and IRAS 16293B; according to Garrod et al. (2022) this could be due to an inaccurate estimate of some activation-energy barriers or to the presence of other pathways for its production not present in the chemical network.

Overall, the agreement of the absolute values of the abundances derived in G31 with those of the slow and medium models is noteworthy. A good agreement for high-mass star-forming regions was found also for SgrB2(N2) with the slow model. However, for some molecular species the agreement was

between the trend seen in the model and in the source among different COMs, while a significant fraction of COMs have absolute values that do not match the model predictions well (Garrod et al. 2022), unlike the case of G31.

5. Conclusions

With the aim of characterizing the emission of the chemically rich HMC G31, and of understanding whether chemical differentiation is present in this source, we analyzed nine O-bearing and six N-bearing COMs using the data of the GUAPOS survey (Mininni et al. 2020; Colzi et al. 2021). Beltrán et al. (2021) highlighted the presence of four sources (labeled A, B, C, and D) when observing this region at high angular resolution, which makes G31 an ideal laboratory to test whether different sources embedded in the same core show different chemistry. The analysis was performed using the SLIM tool within the MADCUBA package. The molecular species analyzed include methanol, CH_3OH, and its isotopologs $^{13}CH_3OH$ and $CH_3^{18}OH$; acetaldehyde, CH_3CHO; dimethyl ether, CH_3OCH_3; acetone, CH_3COCH_3; ethanol, C_2H_5OH; methyl cyanide, CH_3CN; and its isotopologs $^{13}CH_3CN$ and $CH_3^{13}CN$; vinyl cyanide, C_2H_3CN; and ethyl cyanide, C_2H_5CN, and its isotopolog, $C_2H_5^{13}CN$. Moreover, we included in the analysis the three O-bearing isomers of $C_2H_4O_2$, and the O- and N-bearing COMs CH_3NCO, NH_2CHO, $CH_2C(O)NH_2$, and CH_3NHCHO, presented in previous work by Mininni et al. (2020) and Colzi et al. (2021).

The resolution of the maps in not sufficient to give conclusive results on the chemical segregation of molecules in G31. However, from the spectral analysis the most reliable parameter that can show hints of possible chemical differentiation is $V - V_0$. In G31 we find that the values of $V - V_0$ ($V_0 = 96.5\,km\,s^{-1}$) are $\sim 1.0\,km\,s^{-1}$ for the majority of the COMs analyzed in this and previous GUAPOS papers, with the exception of CH_3CHO, CH_3COOH, CH_2OHCHO, and the four O- and N-bearing species CH_3NCO, NH_2CHO, $CH_3C(O)NH_2$, and CH_3NHCHO. In particular, CH_3COOH, CH_2OHCHO, $CH_3C(O)NH_2$, and CH_3NHCHO have $V - V_0$ of ~ 0.2–$0.0\,km\,s^{-1}$, while for CH_3CHO, aGg′-$(CH_2OH)_2$, CH_3NCO, and NH_2CHO the difference is less pronounced, with $V - V_0 \sim 0.5\,km\,s^{-1}$. Considering together the hints from spectral analysis and from map analysis, there are multiple indications of a possible chemical differentiation for the two O-bearing species CH_3CHO and CH_2OHCHO with respect to the other O-bearing species. Other molecules show less pronounced differences in $V - V_0$ and in the shift of the position of the peak.

The values of abundances with respect to H_2 in G31 range from 10^{-6} to 10^{-10} for the different species. We compared the abundances with respect to methanol of O-bearing, N-bearing, and O- and N-bearing COMs in G31 with 27 other sources. These include other high-mass HMCs, hot corinos, shocked regions, the position of envelope gas around a HMC precursor, and molecular clouds. No clear trends among all the HMCs were found. The sources SgrB2-N2/N3/N4/N5 show higher abundances, especially of N-bearing and O- and N-bearing species, when compared to the rest of the HMCs. The abundances (with respect to methanol) found in G31 are in good agreement with those found toward AFGL4176 (Bøgelund et al. 2019), and also the abundances of O-bearing species in G31 are in good agreement with those observed toward Orion-KL in the EG peak (Tercero et al. 2018). However, there is not a unique template for the abundances in HMCs. From the comparison with other types of sources we can see that as a general trend hot corinos show mildly lower abundances with respect to methanol than those in G31, with the exception of the source IRAS 16293–2422 B, while in shocked regions the abundances with respect to methanol are enhanced, thanks to the sputtering of dust grains.

The abundances of COMs in G31 were compared to the results of the three final chemical models of Garrod et al. (2022). The agreement is noteworthy, with most of the species in agreement within a factor of 10 with the estimate by the models. In particular, the slow model shows the best overall agreement, with the exception of $(CH_2OH)_2$, which instead is well reproduced by the medium model. This might indicate that the best model to reproduce the abundances in G31 could have an intermediate timescale between the slow and the medium models, when $(CH_2OH)_2$ is still not heavily destroyed.

Acknowledgements. C.M. acknowledges funding from the European Research Council (ERC) under the European Union's Horizon 2020 program, through the ECOGAL Synergy grant (grant ID 855130). V.M.R. and L.C. have received funding from the Comunidad de Madrid through the Atracción de Talento Investigador (Doctores con experiencia) Grant (COOL: Cosmic Origins Of Life; 2019-T1/TIC-15379). L.C. has also received partial support from the Spanish State Research Agency (AEI; project number PID2019-105552RB-C41). A.S.M. acknowledges support from the RyC2021-032892-I grant funded by MCIN/AEI/10.13039/501100011033 and by the European Union 'Next GenerationEU'/PRTR, as well as the program Unidad de Excelencia María de Maeztu CEX2020-001058-M. This paper makes use of the following ALMA data: ADS/JAO.ALMA#2017.1.00501.S. ALMA is a partnership of ESO (representing its member states), NSF (USA) and NINS (Japan), together with NRC (Canada), MOST and ASIAA (Taiwan), and KASI (Republic of Korea), in cooperation with the Republic of Chile. The Joint ALMA Observatory is operated by ESO, AUI/NRAO and NAOJ.

References

Allen, V., van der Tak, F. F. S., Sánchez-Monge, Á., Cesaroni, R., & Beltrán, M. T. 2017, A&A, 603, A133
Anderson, T., De Lucia, F., & Herbst, E. 1990, ApJS, 72, 797
Ayouz, M. A., Yuen, C. H., Balucani, N., et al. 2019, MNRAS, 490, 1325
Bally, J., & Zinnecker, H. 2005, AJ, 129, 2281
Bally, J., Ginsburg, A., Arce, H., et al. 2017, ApJ, 837, 60
Balucani, N., Ceccarelli, C., & Taquet, V. 2015, MNRAS, 449, L16
Baskakov, O. I., Dyubko, S. F., Ilyushin, V. V., et al. 1996, J. Mol. Spectrosc., 179, 94
Bauer, A., & Godon, M. 1975, Can. J. Phys., 53, 1154
Belloche, A., Müller, H. S. P., Garrod, R. T., & Menten, K. M. 2016, A&A, 587, A91
Belov, S. P., Winnewisser, G., & Herbst, E. 1995, J. Mol. Spectrosc., 174, 253
Beltrán, M. T., Cesaroni, R., Neri, R., et al. 2004, ApJ, 601, L187
Beltrán, M. T., Cesaroni, R., Neri, R., et al. 2005, A&A, 435, 901
Beltrán, M. T., Codella, C., Viti, S., Neri, R., & Cesaroni, R. 2009, ApJ, 690, L93
Beltrán, M. T., Cesaroni, R., Rivilla, V. M., et al. 2018, A&A, 615, A141
Beltrán, M. T., Rivilla, V. M., Cesaroni, R., et al. 2021, A&A, 648, A100
Beltrán, M. T., Rivilla, V. M., Cesaroni, R., et al. 2022a, A&A, 659, A81
Beltrán, M. T., Rivilla, V. M., Kumar, M. S. N., Cesaroni, R., & Galli, D. 2022b, A&A, 660, L4
Bizzocchi, L., Prudenzano, D., Rivilla, V. M., et al. 2020, A&A, 640, A98
Blake, G. A., Sutton, E. C., Masson, C. R., & Phillips, T. G. 1987, ApJ, 315, 621
Bøgelund, E. G., Barr, A. G., Taquet, V., et al. 2019, A&A, 628, A2
Bonato, M., Liuzzo, E., Giannetti, A., et al. 2018, MNRAS, 478, 1512
Bonfand, M., Belloche, A., Garrod, R. T., et al. 2019, A&A, 628, A27
Boucher, D., Burie, J., Demaison, J., et al. 1977, J. Mol. Spectrosc., 64, 290
Boucher, D., Dubrulle, A., Demaison, J., & Dreizler, H. 1980, Z. Naturf. A, 35, 1136
Briggs, D. S. 1995, in Am. Astron. Soc. Meeting Abstracts, 187, 112.02
Calcutt, H., Viti, S., Codella, C., et al. 2014, MNRAS, 443, 3157
Caselli, P., Hasegawa, T. I., & Herbst, E. 1993, ApJ, 408, 548
Cazzoli, G., & Kisiel, Z. 1988, J. Mol. Spectrosc., 130, 303
Cazzoli, G., & Puzzarini, C. 2006, J. Mol. Spectrosc., 240, 153
Cesaroni, R. 2019, A&A, 631, A65
Cesaroni, R., Olmi, L., Walmsley, C. M., Churchwell, E., & Hofner, P. 1994, ApJ, 435, L137
Cesaroni, R., Hofner, P., Araya, E., & Kurtz, S. 2010, A&A, 509, A50

Cesaroni, R., Beltrán, M. T., Zhang, Q., Beuther, H., & Fallscheer, C. 2011, A&A, 533, A73
Cesaroni, R., Sánchez-Monge, Á., Beltrán, M. T., et al. 2017, A&A, 602, A59
Christen, D., & Müller, H. S. P. 2003, Phys. Chem. Chem. Phys. (Incorp. Faraday Trans.), 5, 3600
Christen, D., Coudert, L. H., Suenram, R. D., & Lovas, F. J. 1995, J. Mol. Spectrosc., 172, 57
Christen, D., Coudert, L. H., Larsson, J. A., & Cremer, D. 2001, J. Mol. Spectrosc., 205, 185
Codella, C., Benedettini, M., Beltrán, M. T., et al. 2009, A&A, 507, L25
Colmont, J. M., Wlodarczak, G., Priem, D., et al. 1997, J. Mol. Spectrosc., 181, 330
Colzi, L., Rivilla, V. M., Beltrán, M. T., et al. 2021, A&A, 653, A129
Coutens, A., Jørgensen, J. K., van der Wiel, M. H. D., et al. 2016, A&A, 590, L6
Crockett, N. R., Bergin, E. A., Neill, J. L., et al. 2015, ApJ, 806, 239
Csengeri, T., Belloche, A., Bontemps, S., et al. 2019, A&A, 632, A57
Demaison, J., Dubrulle, A., Boucher, D., Burie, J., & Typke, V. 1979, J. Mol. Spectrosc., 76, 1
Demaison, J., Cosleou, J., Bocquet, R., & Lesarri, A. G. 1994, J. Mol. Spectrosc., 167, 400
Demyk, K., Mäder, H., Tercero, B., et al. 2007, A&A, 466, 255
Durig, J. R., Deeb, H., Darkhalil, I. D., et al. 2011, J. Mol. Struct., 985, 202
Endres, C. P., Drouin, B. J., Pearson, J. C., et al. 2009, A&A, 504, 635
Feng, S., Beuther, H., Henning, T., et al. 2015, A&A, 581, A71
Fisher, J., Paciga, G., Xu, L.-H., et al. 2007, J. Mol. Spectrosc., 245, 7
Fontani, F., Pascucci, I., Caselli, P., et al. 2007, A&A, 470, 639
Friedel, D. N., & Snyder, L. E. 2008, ApJ, 672, 962
Fukuyama, Y., Odashima, H., Takagi, K., & Tsunekawa, S. 1996, ApJS, 104, 329
García de la Concepción, J., Colzi, L., Jiménez-Serra, I., et al. 2022, A&A, 658, A150
Garrod, R. T. 2013, ApJ, 765, 60
Garrod, R. T., Jin, M., Matis, K. A., et al. 2022, ApJS, 259, 1
Gerry, M. C. L., & Winnewisser, G. 1973, J. Mol. Spectrosc., 48, 1
Gerry, M. C. L., Lees, R. M., & Winnewisser, G. 1976, J. Mol. Spectrosc., 61, 231
Girart, J. M., Beltrán, M. T., Zhang, Q., Rao, R., & Estalella, R. 2009, Science, 324, 1408
Gorai, P., Das, A., Shimonishi, T., et al. 2021, ApJ, 907, 108
Groner, P., Albert, S., Herbst, E., & De Lucia, F. C. 1998, ApJ, 500, 1059
Groner, P., Albert, S., Herbst, E., et al. 2002, ApJS, 142, 145
Herbst, E., & van Dishoeck, E. F. 2009, ARA&A, 47, 427
Herbst, E., Messer, J. K., De Lucia, F. C., & Helminger, P. 1984, J. Mol. Spectrosc., 108, 42
Hoshino, Y., Ohishi, M., Akabane, K., et al. 1996, ApJS, 104, 317
Hughes, R. H., Good, W. E., & Coles, D. K. 1951, Phys. Rev., 84, 418
Ikeda, M., Duan, Y.-B., Tsunekawa, S., & Takagi, K. 1998, ApJS, 117, 249
Immer, K., Li, J., Quiroga-Nuñez, L. H., et al. 2019, A&A, 632, A123
Isokoski, K., Bottinelli, S., & van Dishoeck, E. F. 2013, A&A, 554, A100
Jiménez-Serra, I., Zhang, Q., Viti, S., Martín-Pintado, J., & de Wit, W. J. 2012, ApJ, 753, 34
Jiménez-Serra, I., Vasyunin, A. I., Caselli, P., et al. 2016, ApJ, 830, L6
Johnson, D. R., Lovas, F. J., Gottlieb, C. A., et al. 1977, ApJ, 218, 370
Jørgensen, J. K., van der Wiel, M. H. D., Coutens, A., et al. 2016, A&A, 595, A117
Jørgensen, J. K., Müller, H. S. P., Calcutt, H., et al. 2018, A&A, 620, A170
Kalenskii, S. V., & Johansson, L. E. B. 2010, Astron. Rep., 54, 1084
Kleiner, I., Lovas, F. J., & Godefroid, M. 1996, J. Phys. Chem. Ref. Data, 25, 1113
Kukolich, S. G. 1982, J. Chem. Phys., 76, 97
Kukolich, S. G., Ruben, D. J., Wang, J. H. S., & Williams, J. R. 1973, J. Chem. Phys., 58, 3155
Lees, R. M., & Baker, J. G. 1968, J. Chem. Phys., 48, 5299
Lefloch, B., Ceccarelli, C., Codella, C., et al. 2017, MNRAS, 469, L73
López-Sepulcre, A., Sakai, N., Neri, R., et al. 2017, A&A, 606, A121
Lovas, F. J., Lutz, H., & Dreizler, H. 1979, J. Phys. Chem. Ref. Data, 8, 1051
Lykke, J. M., Coutens, A., Jørgensen, J. K., et al. 2017, A&A, 597, A53
Mäder, H., Heise, H. M., & Dreizler, H. 1974, Z. Naturf. A, 29, 164
Manigand, S., Jørgensen, J. K., Calcutt, H., et al. 2020, A&A, 635, A48
Martín, S., Requena-Torres, M. A., Martín-Pintado, J., & Mauersberger, R. 2008, ApJ, 678, 245
Martín, S., Martín-Pintado, J., Blanco-Sánchez, C., et al. 2019, A&A, 631, A159
Matsushima, F., Evenson, K. M., & Zink, L. R. 1994, J. Mol. Spectrosc., 164, 517
Mayen-Gijon, J. M., Anglada, G., Osorio, M., et al. 2014, MNRAS, 437, 3766
McMullin, J. P., Waters, B., Schiebel, D., Young, W., & Golap, K. 2007, ASP Conf. Ser., 376, CASA Architecture and Applications, eds. R. A. Shaw, F. Hill, & D. J. Bell, 127
Mininni, C., Fontani, F., Rivilla, V. M., et al. 2018, MNRAS, 476, L39
Mininni, C., Beltrán, M. T., Rivilla, V. M., et al. 2020, A&A, 644, A84
Müller, H. S. P., & Christen, D. 2004, J. Mol. Spectrosc., 228, 298
Müller, H. S. P., Thorwirth, S., Roth, D. A., & Winnewisser, G. 2001, A&A, 370, L49
Müller, H. S. P., Menten, K. M., & Mäder, H. 2004, A&A, 428, 1019
Müller, H. S. P., Schlöder, F., Stutzki, J., & Winnewisser, G. 2005, J. Mol. Struct., 742, 215
Müller, H. S. P., Belloche, A., Menten, K. M., Comito, C., & Schilke, P. 2008, J. Mol. Spectrosc., 251, 319
Müller, H. S. P., Drouin, B. J., & Pearson, J. C. 2009, A&A, 506, 1487
Müller, H. S. P., Brown, L. R., Drouin, B. J., et al. 2015, J. Mol. Spectrosc., 312, 22
Müller, H. S. P., Belloche, A., Xu, L.-H., et al. 2016, A&A, 587, A92
Nazari, P., van Gelder, M. L., van Dishoeck, E. F., et al. 2021, A&A, 650, A150
Neustock, W., Guarnieri, A., Demaison, J., & Wlodarczak, G. 1990, Z. Naturf. A, 45, 702
Odashima, H., Matsushima, F., Nagai, K., Tsunekawa, S., & Takagi, K. 1995, J. Mol. Spectrosc., 173, 404
Oldag, F., & Sutter, D. H. 1992, Z. Naturf. A, 47, 527
Osorio, M., Anglada, G., Lizano, S., & D'Alessio, P. 2009, ApJ, 694, 29
Pagani, L., Bergin, E., Goldsmith, P. F., et al. 2019, A&A, 624, L5
Palau, A., Fuente, A., Girart, J. M., et al. 2011, ApJ, 743, L32
Pearson, J. C., & Mueller, H. S. P. 1996, ApJ, 471, 1067
Pearson, J. C., Sastry, K. V. L. N., Herbst, E., & De Lucia, F. C. 1994, ApJS, 93, 589
Pearson, J. C., Sastry, K. V. L. N., Winnewisser, M., Herbst, E., & De Lucia, F. C. 1995, J. Phys. Chem. Ref. Data, 24, 1
Pearson, J. C., Brauer, C. S., & Drouin, B. J. 2008, J. Mol. Spectrosc., 251, 394
Peng, T. C., Despois, D., Brouillet, N., et al. 2013, A&A, 554, A78
Peng, Y., Liu, T., Qin, S.-L., et al. 2022, MNRAS, 512, 4419
Peter, R., & Dreizler, H. 1965, Z. Naturf. A, 20, 301
Pickett, H. M., Cohen, E. A., Brinza, D. E., & Schaefer, M. M. 1981, J. Mol. Spectrosc., 89, 542
Pickett, H. M., Poynter, R. L., Cohen, E. A., et al. 1998, J. Quant. Spec. Radiat. Transf., 60, 883
Predoi-Cross, A., Lees, R. M., Lichau, H., Winnewisser, M., & Drummond, J. R. 1997, Int. J. Infrared Millimeter Waves, 18, 2047
Qin, S.-L., Liu, T., Liu, X., et al. 2022, MNRAS, 511, 3463
Remijan, A., Shiao, Y. S., Friedel, D. N., Meier, D. S., & Snyder, L. E. 2004, ApJ, 617, 384
Requena-Torres, M. A., Martín-Pintado, J., Rodríguez-Franco, A., et al. 2006, A&A, 455, 971
Requena-Torres, M. A., Martín-Pintado, J., Martín, S., & Morris, M. R. 2008, ApJ, 672, 352
Richard, C., Margulès, L., Motiyenko, R. A., & Guillemin, J. C. 2012, A&A, 543, A135
Rivilla, V. M., Beltrán, M. T., Cesaroni, R., et al. 2017, A&A, 598, A59
Rivilla, V. M., Colzi, L., Jiménez-Serra, I., et al. 2022, ApJ, 929, L11
Rodríguez-Almeida, L. F., Jiménez-Serra, I., Rivilla, V. M., et al. 2021, ApJ, 912, L11
Sánchez-Monge, Á., Schilke, P., Ginsburg, A., Cesaroni, R., & Schmiedeke, A. 2018, A&A, 609, A101
Sanz-Novo, M., Belloche, A., Rivilla, V. M., et al. 2022, A&A, 666, A114
Sastry, K. V. L. N., Lees, R. M., & De Lucia, F. C. 1984, J. Mol. Spectrosc., 103, 486
Sipilä, O., Silsbee, K., & Caselli, P. 2021, ApJ, 922, 126
Stolze, M., & Sutter, D. H. 1985, Z. Naturf. A, 40, 998
Suzuki, T., Majumdar, L., Ohishi, M., et al. 2018, ApJ, 863, 51
Taquet, V., Bianchi, E., Codella, C., et al. 2019, A&A, 632, A19
Tercero, B., Cuadrado, S., López, A., et al. 2018, A&A, 620, A6
Vacherand, J. M., Van Eijck, B. P., Burie, J., & Demaison, J. 1986, J. Mol. Spectrosc., 118, 355
van der Walt, S. J., Kristensen, L. E., Jørgensen, J. K., et al. 2021, A&A, 655, A86
van Gelder, M. L., Tabone, B., Tychoniec, Ł., et al. 2020, A&A, 639, A87
Viti, S., & Williams, D. A. 1999, MNRAS, 305, 755
Viti, S., Collings, M. P., Dever, J. W., McCoustra, M. R. S., & Williams, D. A. 2004, MNRAS, 354, 1141
Widicus Weaver, S. L., & Friedel, D. N. 2012, ApJS, 201, 16
Widicus Weaver, S. L., Laas, J. C., Zou, L., et al. 2017, ApJS, 232, 3
Wilson, T. L., & Rood, R. 1994, ARA&A, 32, 191
Wyrowski, F., Schilke, P., Walmsley, C. M., & Menten, K. M. 1999, ApJ, 514, L43
Xu, L.-H., & Lovas, F. J. 1997, J. Phys. Chem. Ref. Data, 26, 17
Xu, L.-H., Fisher, J., Lees, R. M., et al. 2008, J. Mol. Spectrosc., 251, 305
Yan, Y. T., Zhang, J. S., Henkel, C., et al. 2019, ApJ, 877, 154
Zeng, S., Jiménez-Serra, I., Rivilla, V. M., et al. 2018, MNRAS, 478, 2962
Zernickel, A., Schilke, P., Schmiedeke, A., et al. 2012, A&A, 546, A87

Appendix A: Documentation of catalog entries for the molecular species analyzed

Appendix A.1: Methanol CH_3OH, $^{13}CH_3OH$, and $CH_3^{18}OH$

We used the spectroscopy from the CDMS catalog. The entry of CH_3OH is based mainly on the work of Xu et al. (2008), with additional data from Lees & Baker (1968), Pickett et al. (1981), Sastry et al. (1984), Herbst et al. (1984), Anderson et al. (1990), Matsushima et al. (1994), Odashima et al. (1995), Belov et al. (1995), and Müller et al. (2004). More information is available at
https://cdms.astro.uni-koeln.de/cgi-bin/cdmsinfo?file=e032504.cat

The entry of $^{13}CH_3OH$ is based on the review work by Xu & Lovas (1997). More information available at
https://cdms.astro.uni-koeln.de/cgi-bin/cdmsinfo?file=e033502.cat

The entry of $CH_3^{18}OH$ is based on the work by Fisher et al. (2007) with the inclusion of other transitions from Hughes et al. (1951), Gerry et al. (1976), Hoshino et al. (1996), Predoi-Cross et al. (1997), and Ikeda et al. (1998). More information available at
https://cdms.astro.uni-koeln.de/cgi-bin/cdmsinfo?file=e034504.cat

Appendix A.2: Acetaldehyde CH_3CHO

We used the spectroscopy from the JPL catalog. The entry is based on the work of Kleiner et al. (1996) and references therein. More information is available at
https://spec.jpl.nasa.gov/ftp/pub/catalog/doc/d044003.pdf

Appendix A.3: Dimethyl ether CH_3OCH_3

We used the spectroscopy from the CDMS catalog. The entry of CH_3OCH_3 is based mainly on the work of Endres et al. (2009), Lovas et al. (1979), Neustock et al. (1990), and Groner et al. (1998). More information is available at
https://cdms.astro.uni-koeln.de/cgi-bin/cdmsinfo?file=e046514.cat

Appendix A.4: Acetone CH_3COCH_3

We used the spectroscopy from the JPL catalog. The entry is based on the works of Peter & Dreizler (1965), Vacherand et al. (1986), Oldag & Sutter (1992), and Groner et al. (2002). More information is available at
https://spec.jpl.nasa.gov/ftp/pub/catalog/doc/d058003.pdf

Appendix A.5: Ethanol C_2H_5OH

We used the spectroscopy from the CDMS catalog. The entry of C_2H_5OH is based mainly on the work of Pearson et al. (1995); Pearson & Mueller (1996); Pearson et al. (2008). More information is available at
https://cdms.astro.uni-koeln.de/cgi-bin/cdmsinfo?file=e046524.cat

Appendix A.6: Ethylene glycol aGg′-$(CH_2OH)_2$ and gGg′-$(CH_2OH)_2$

We used the spectroscopy from the CDMS catalog. The entries of aGg′-$(CH_2OH)_2$ is based on the works by Christen et al. (1995) and Christen & Müller (2003). More information is available at
https://cdms.astro.uni-koeln.de/cgi-bin/cdmsinfo?file=e062503.cat

The entries of gGg′-$(CH_2OH)_2$ is based on the works by Christen et al. (2001) and Müller & Christen (2004). More information is available at
https://cdms.astro.uni-koeln.de/cgi-bin/cdmsinfo?file=e062504.cat

Appendix A.7: Methyl cyanide CH_3CN, $^{13}CH_3CN$, and $CH_3^{13}CN$

We used the spectroscopy from the CDMS catalog. The entry of CH_3CN is mainly based on the works by Müller et al. (2015), Kukolich et al. (1973); Kukolich (1982), Boucher et al. (1977), Cazzoli & Puzzarini (2006), and Bauer & Godon (1975). More information is available at
https://cdms.astro.uni-koeln.de/cgi-bin/cdmsinfo?file=e041505.cat

The entry of $^{13}CH_3CN$ is based on the works by Müller et al. (2009), Pearson & Mueller (1996), and Demaison et al. (1979). More information is available at
https://cdms.astro.uni-koeln.de/cgi-bin/cdmsinfo?file=e042508.cat

The entry of $CH_3^{13}CN$ is a combined CDMS and JPL entry, and is based on the works by Müller et al. (2009), Pearson & Mueller (1996), Demaison et al. (1979), and Kukolich (1982). More information is available at
https://cdms.astro.uni-koeln.de/cgi-bin/cdmsinfo?file=e042509.cat

Appendix A.8: Vinyl cyanide C_2H_3CN

We used the spectroscopy from the CDMS catalog. The entry of C_2H_3CN is based mainly on the works of Müller et al. (2008), Gerry & Winnewisser (1973), Stolze & Sutter (1985), Cazzoli & Kisiel (1988), Demaison et al. (1994), Baskakov et al. (1996), and Colmont et al. (1997). More information is available at
https://cdms.astro.uni-koeln.de/cgi-bin/cdmsinfo?file=e053515.cat

Appendix A.9: Ethyl cyanide C_2H_5CN and $C_2H_5^{13}CN$

We used the spectroscopy from the CDMS catalog. The entry of C_2H_5CN is based mainly on the works of Mäder et al. (1974), Johnson et al. (1977), Boucher et al. (1980), Pearson et al. (1994), and Fukuyama et al. (1996). More information is available at
https://cdms.astro.uni-koeln.de/cgi-bin/cdmsinfo?file=e055502.cat

The entry of $C_2H_5^{13}CN$ is based mainly on the works of Demyk et al. (2007) and Richard et al. (2012). More information is available at
https://cdms.astro.uni-koeln.de/cgi-bin/cdmsinfo?file=e056504.cat

Appendix B: Spectra

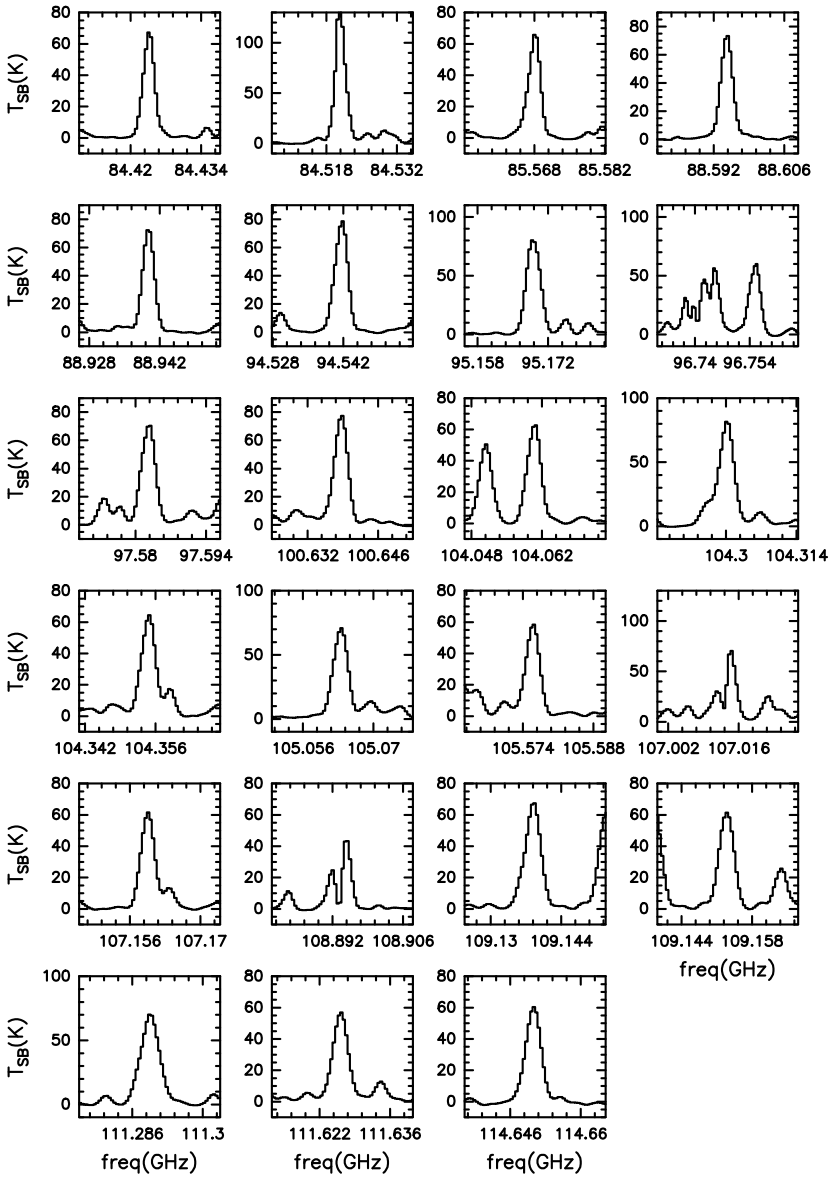

Fig. B.1. Observed spectrum of some of the brightest transitions of CH_3OH $v_t = 0$. T_{SB} stands for synthesized beam temperature.

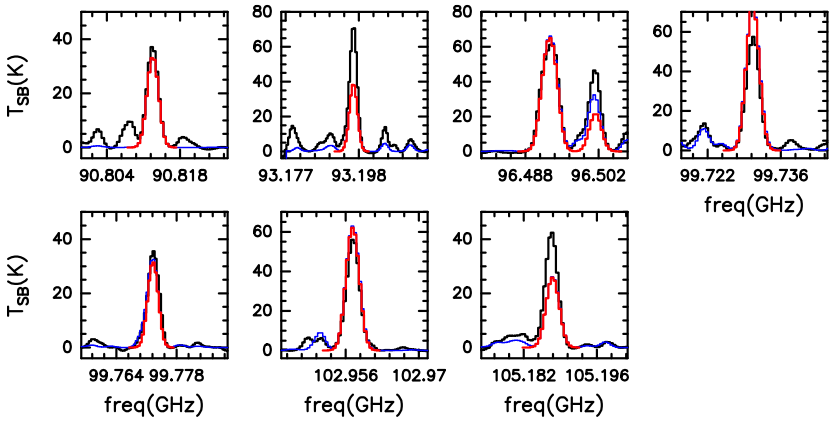

Fig. B.2. Transitions used to constrain the fit of CH_3OH $v_t = 1$. Shown in black is the observed spectrum, in red the synthetic spectrum of the best fit for CH_3OH $v_t = 1$ only, and in blue the spectrum that takes into account all the species identified in the spectrum, including those published in Mininni et al. (2020); Colzi et al. (2021). T_{SB} stands for synthesized beam temperature.

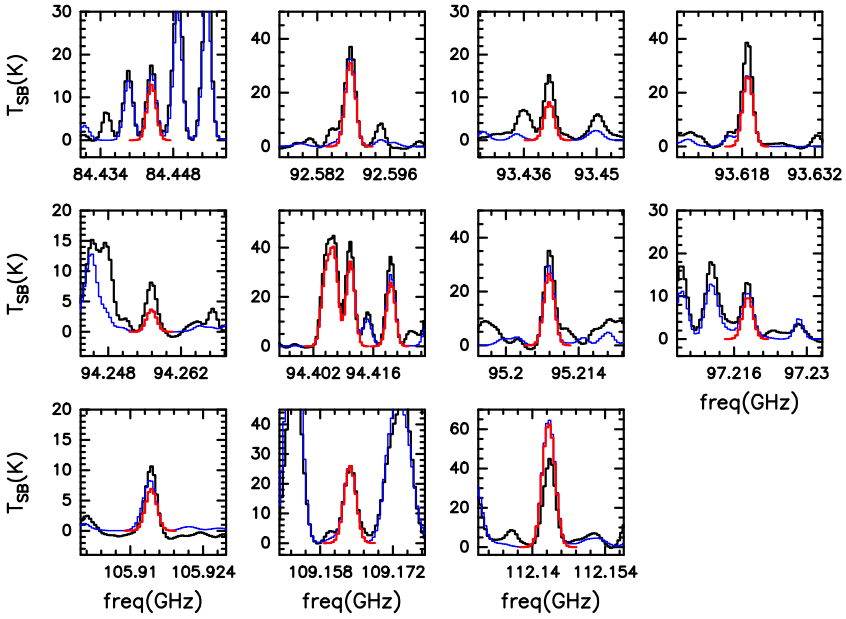

Fig. B.3. Transitions used to constrain the fit of $^{13}CH_3OH$. Shown in black is the observed spectrum, in red the synthetic spectrum of the best fit for $^{13}CH_3OH$ only, and in blue the spectrum that takes into account all the species identified in the spectrum, including those published in Mininni et al. (2020); Colzi et al. (2021). T_{SB} stands for synthesized beam temperature.

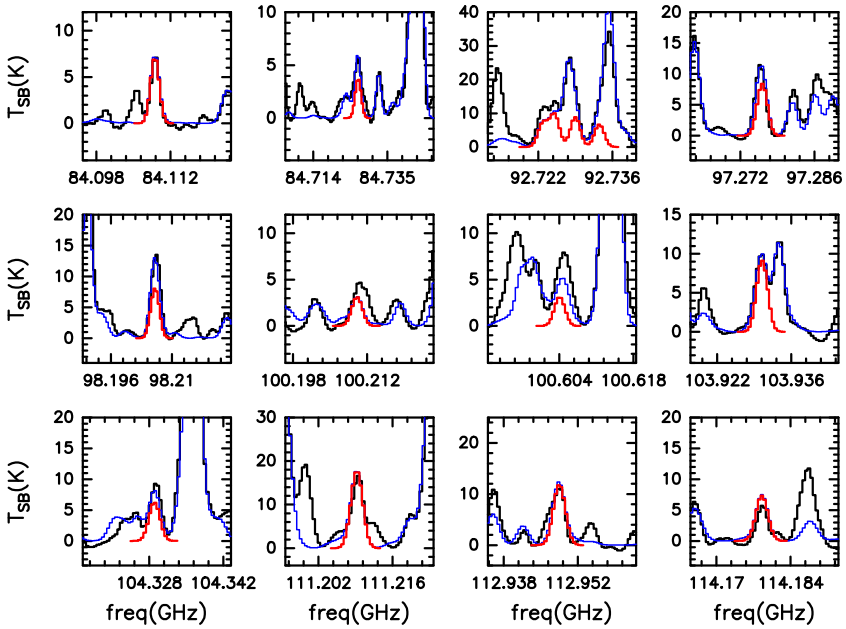

Fig. B.4. Transitions used to constrain the fit of $CH_3^{18}OH$. Shown in black is the observed spectrum, in red the synthetic spectrum of the best fit for $CH_3^{18}OH$ only, and in blue the spectrum that takes into account all the species identified in the spectrum, including those published in Mininni et al. (2020); Colzi et al. (2021). T_{SB} stands for synthesized beam temperature.

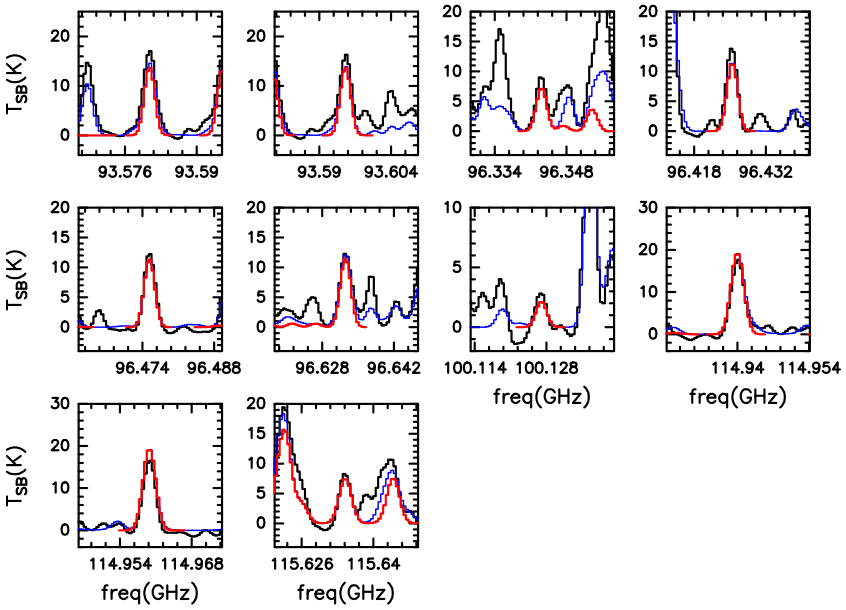

Fig. B.5. Transitions used to constrain the fit of CH_3CHO. Shown in black is the observed spectrum, in red the synthetic spectrum of the best fit for CH_3CHO only, and in blue the spectrum that takes into account all the species identified in the spectrum, including those published in Mininni et al. (2020); Colzi et al. (2021). T_{SB} stands for synthesized beam temperature.

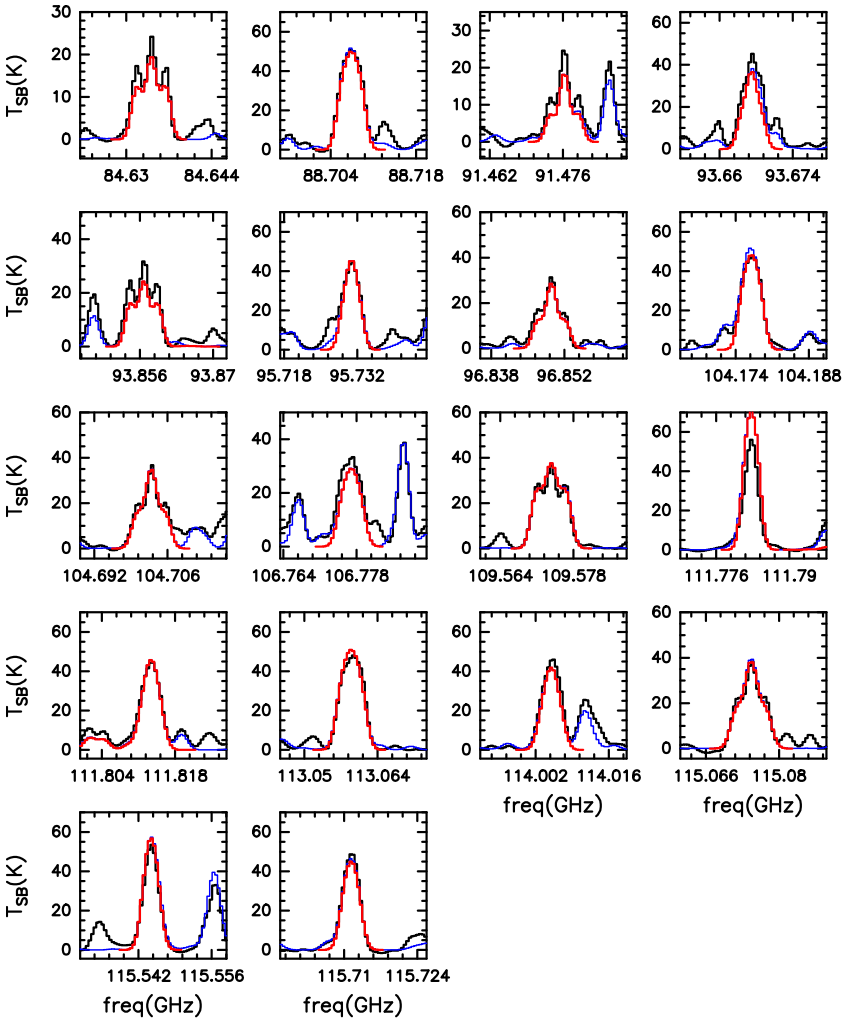

Fig. B.6. Transitions used to constrain the fit of CH_3OCH_3. Shown in black is the observed spectrum, in red the synthetic spectrum of the best fit for CH_3OCH_3 only, and in blue the spectrum that takes into account all the species identified in the spectrum, including those published in Mininni et al. (2020); Colzi et al. (2021). T_{SB} stands for synthesized beam temperature.

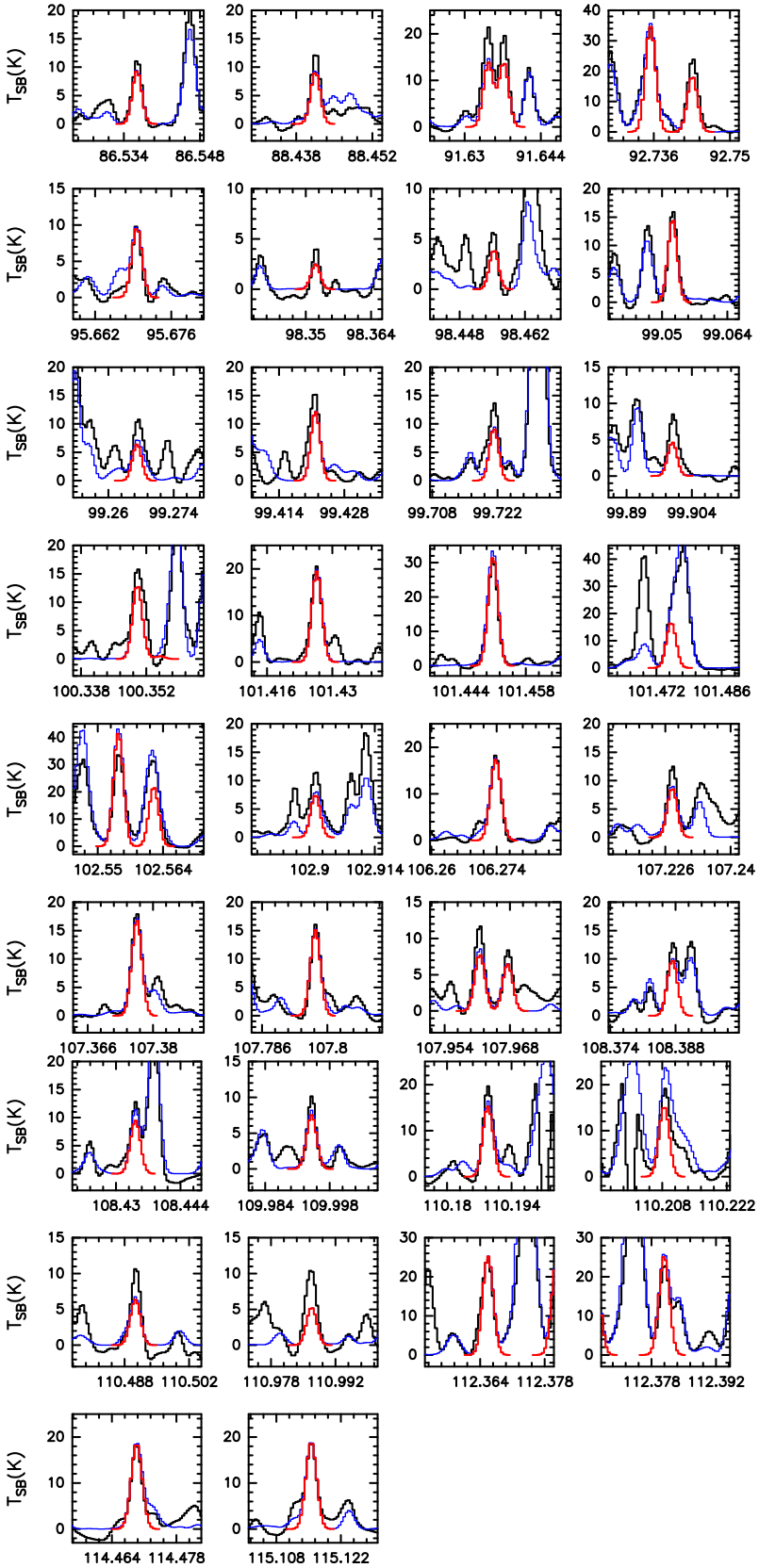

Fig. B.7. Transitions used to constrain the fit of CH_3COCH_3. Shown in black is the observed spectrum, in red the synthetic spectrum of the best fit for CH_3COCH_3 only, and in blue the spectrum that takes into account all the species identified in the spectrum, including those published in Mininni et al. (2020); Colzi et al. (2021). T_{SB} stands for synthesized beam temperature.

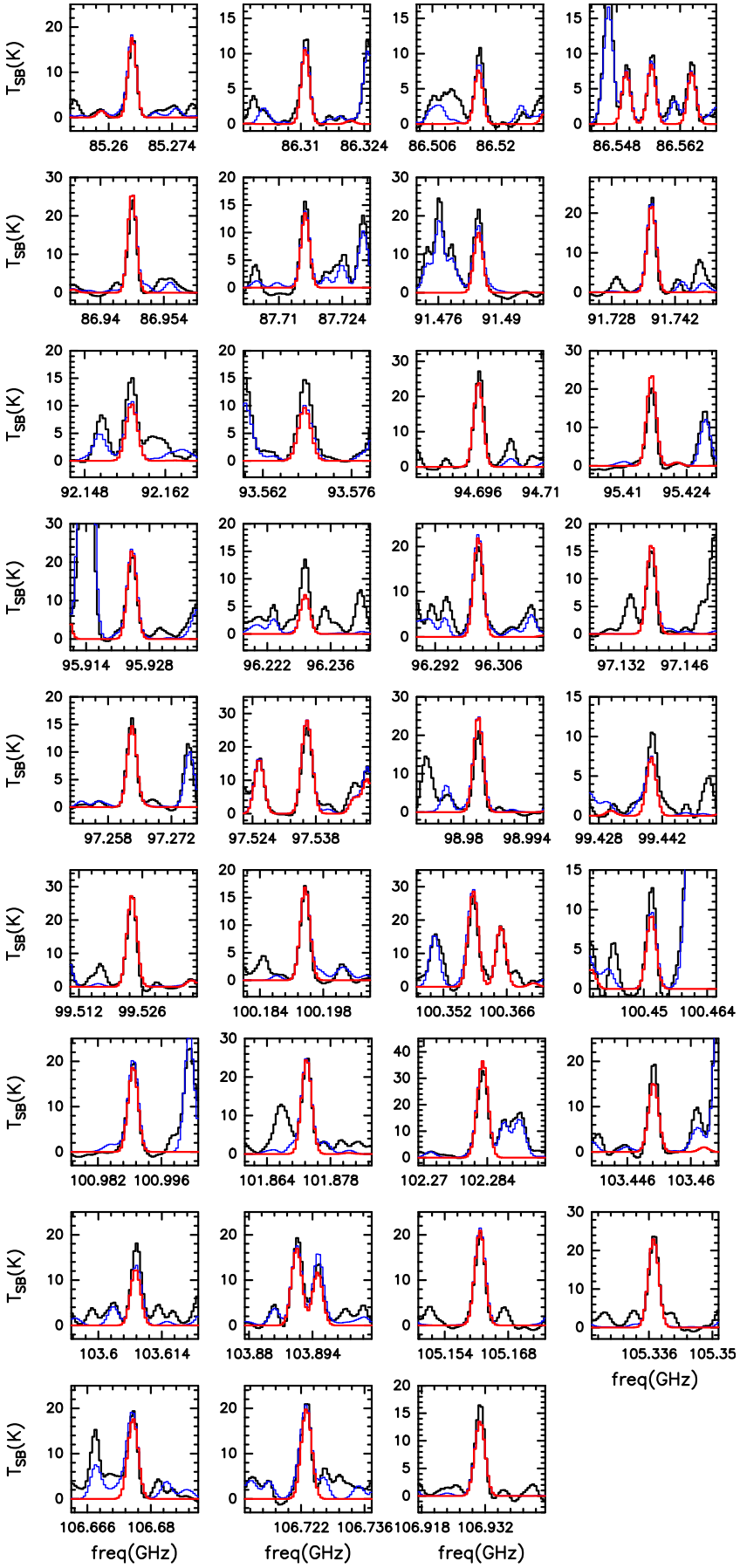

Fig. B.8. Transitions used to constrain the fit of C_2H_5OH. Shown in black is the observed spectrum, in red the synthetic spectrum of the best fit for C_2H_5OH only, and in blue the spectrum that takes into account all the species identified in the spectrum, including those published in Mininni et al. (2020); Colzi et al. (2021). T_{SB} stands for synthesized beam temperature.

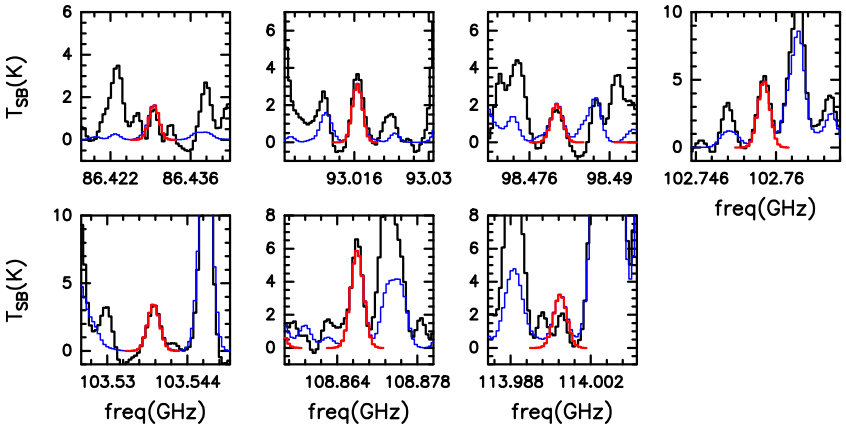

Fig. B.9. Transitions used to constrain the fit of gGg′-$(CH_2OH)_2$. Shown in black is the observed spectrum, in red the synthetic spectrum of the best fit for gGg′-$(CH_2OH)_2$ only, and in blue the spectrum that takes into account all the species identified in the spectrum, including those published in Mininni et al. (2020); Colzi et al. (2021). T_{SB} stands for synthesized beam temperature.

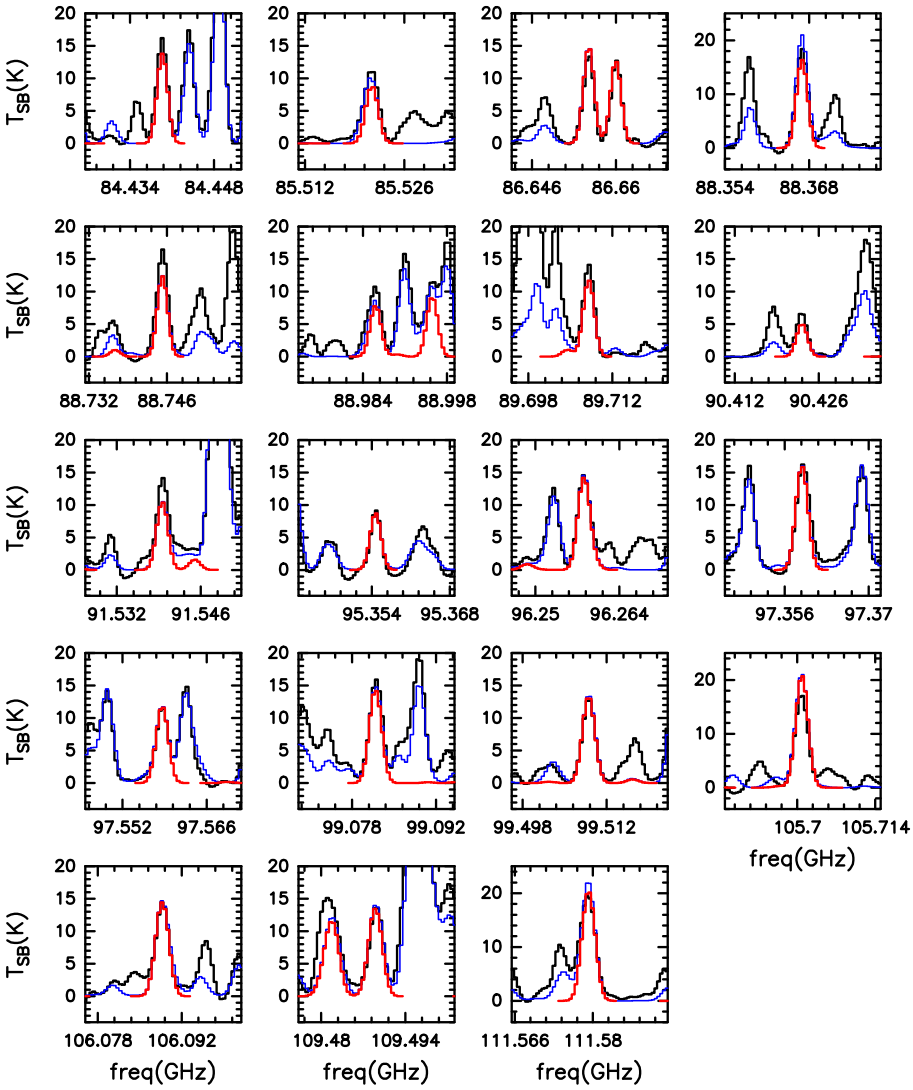

Fig. B.10. Transitions used to constrain the fit of aGg′-$(CH_2OH)_2$. Shown in black the observed spectrum, in red the synthetic spectrum of the best fit for aGg′-$(CH_2OH)_2$ only, and in blue the spectrum that takes into account all the species identified in the spectrum, including those published in Mininni et al. (2020); Colzi et al. (2021). T_{SB} stands for synthesized beam temperature.

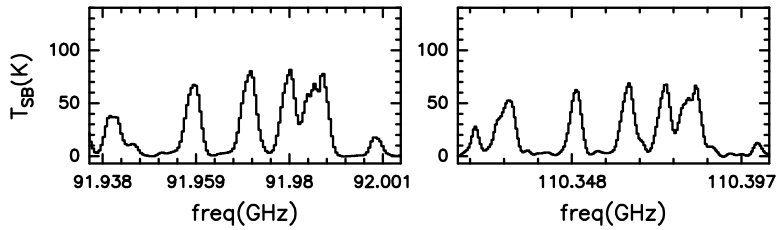

Fig. B.11. Observed spectrum of CH_3CN v=0. T_{SB} stands for synthesized beam temperature.

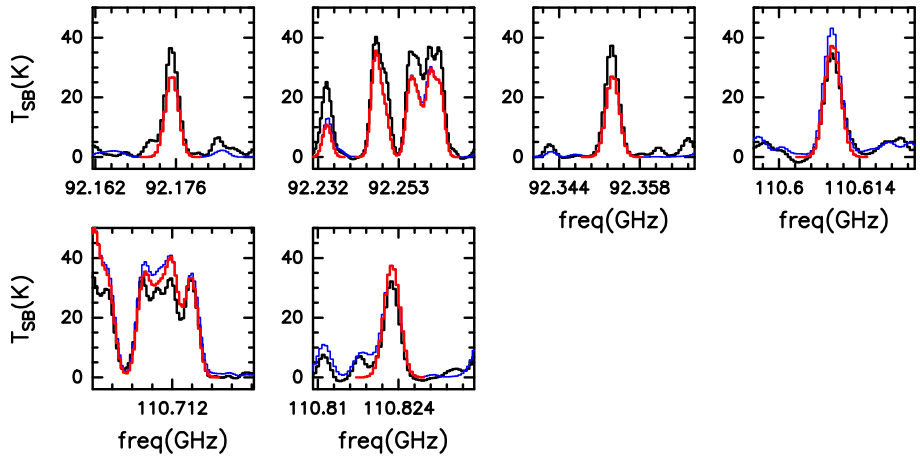

Fig. B.12. Transitions used to constrain the fit of CH_3CN $v_8 = 1$. Shown in black the observed spectrum, in red the synthetic spectrum of the best fit for CH_3CN $v_8 = 1$ only, and in blue the spectrum that takes into account all the species identified in the spectrum, including those published in Mininni et al. (2020); Colzi et al. (2021). T_{SB} stands for synthesized beam temperature.

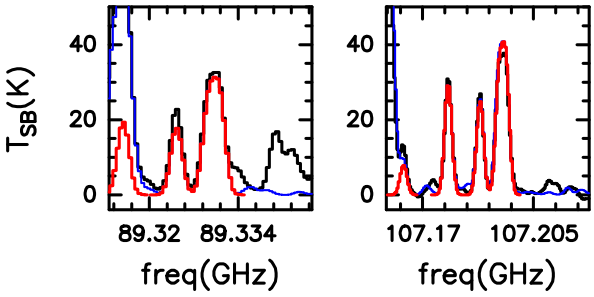

Fig. B.13. Transitions used to constrain the fit of $^{13}CH_3CN$. Shown in black the observed spectrum, in red the synthetic spectrum of the best fit for $^{13}CH_3CN$ only, and in blue the spectrum that takes into account all the species identified in the spectrum, including those published in Mininni et al. (2020); Colzi et al. (2021). T_{SB} stands for synthesized beam temperature.

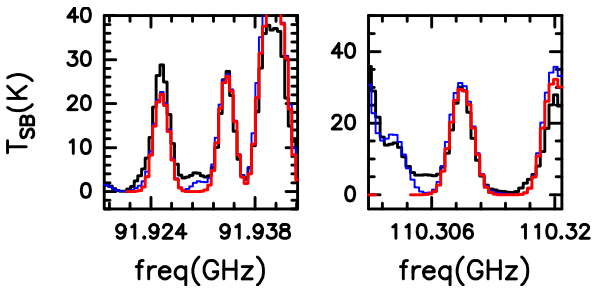

Fig. B.14. Transitions used to constrain the fit of $CH_3^{13}CN$. Shown in black is the observed spectrum, in red the synthetic spectrum of the best fit for $CH_3^{13}CN$ only, and in blue the spectrum that takes into account all the species identified in the spectrum, including those published in Mininni et al. (2020); Colzi et al. (2021). T_{SB} stands for synthesized beam temperature.

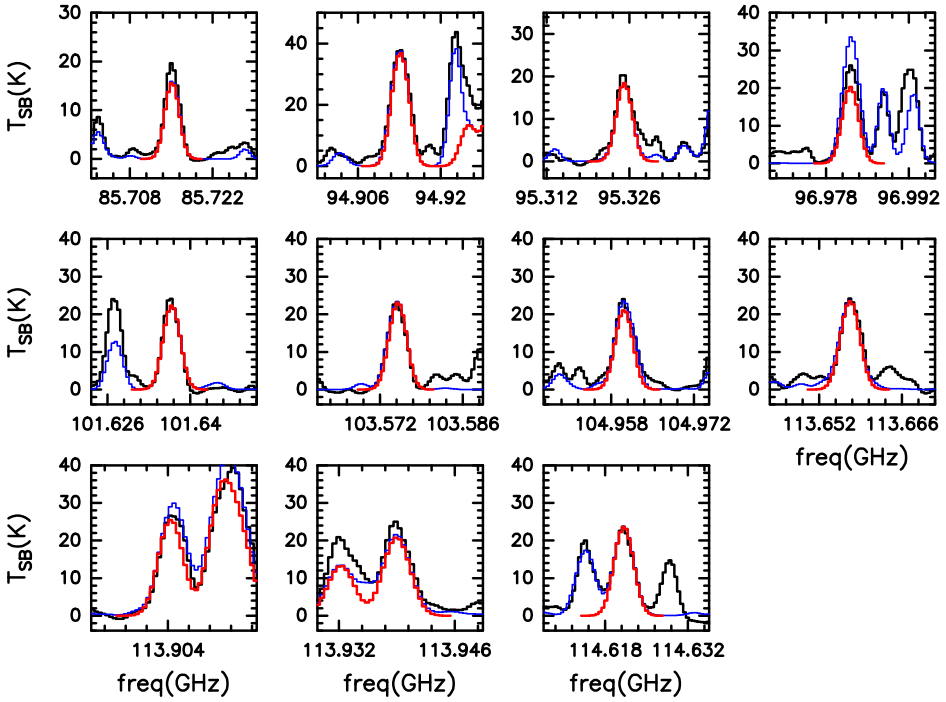

Fig. B.15. Transitions used to constrain the fit of C_2H_3CN. Shown in black is the observed spectrum, in red the synthetic spectrum of the best fit for C_2H_3CN only, and in blue the spectrum that takes into account all the species identified in the spectrum, including those published in Mininni et al. (2020); Colzi et al. (2021). T_{SB} stands for synthesized beam temperature.

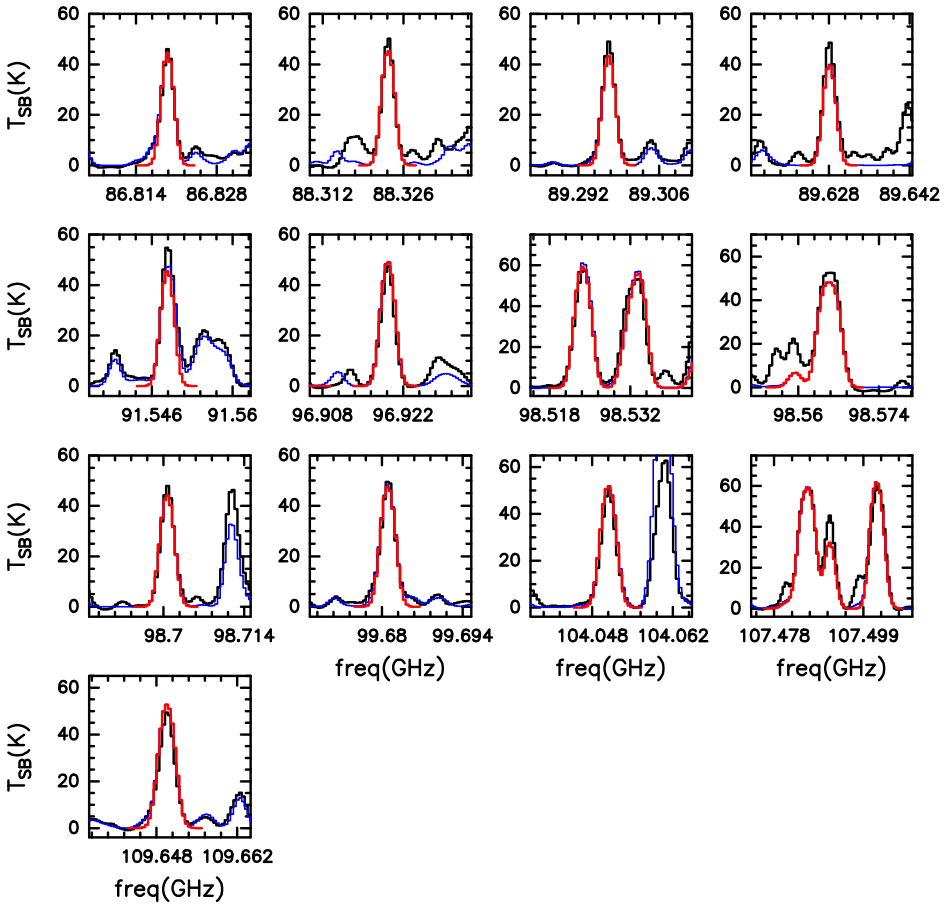

Fig. B.16. Transitions used to constrain the fit of C_2H_5CN. Shown in black is the observed spectrum, in red the synthetic spectrum of the best fit for C_2H_5CN only, and in blue the spectrum that takes into account all the species identified in the spectrum, including those published in Mininni et al. (2020); Colzi et al. (2021). T_{SB} stands for synthesized beam temperature.

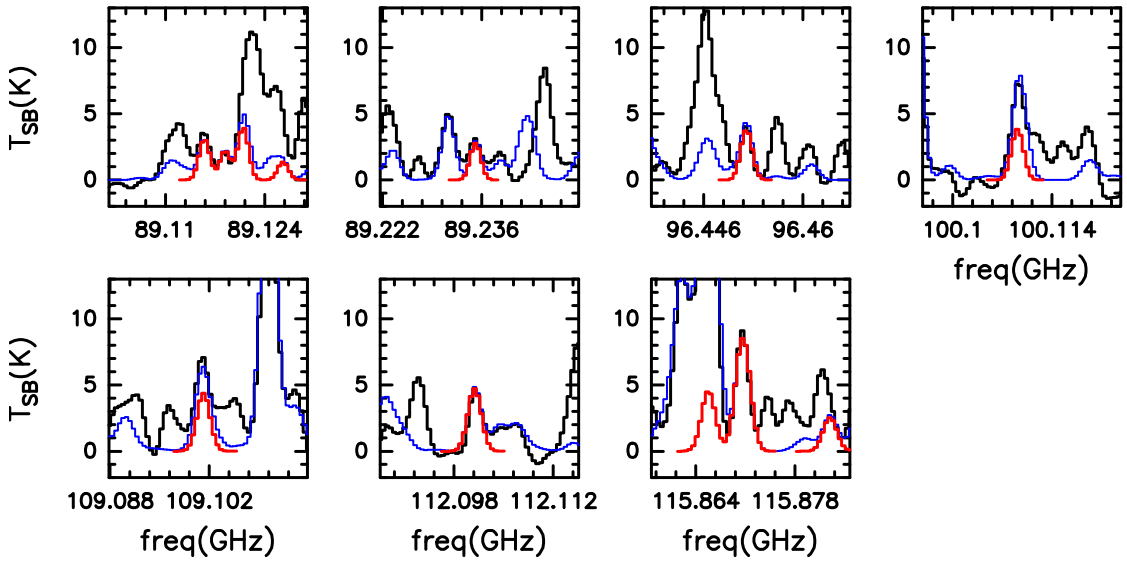

Fig. B.17. Transitions used to constrain the fit of $C_2H_5^{13}CN$. Shown in black is the observed spectrum, in red the synthetic spectrum of the best fit for $C_2H_5^{13}CN$ only, while in blue the spectrum that takes into account all the species identified in the spectrum, including those published in Mininni et al. (2020); Colzi et al. (2021). T_{SB} stands for synthesized beam temperature.

Appendix C: Selected transitions for the analysis

Tables C.1 to C.15 are only available in electronic form at the CDS.

Appendix D: Moment maps of low-energy transitions

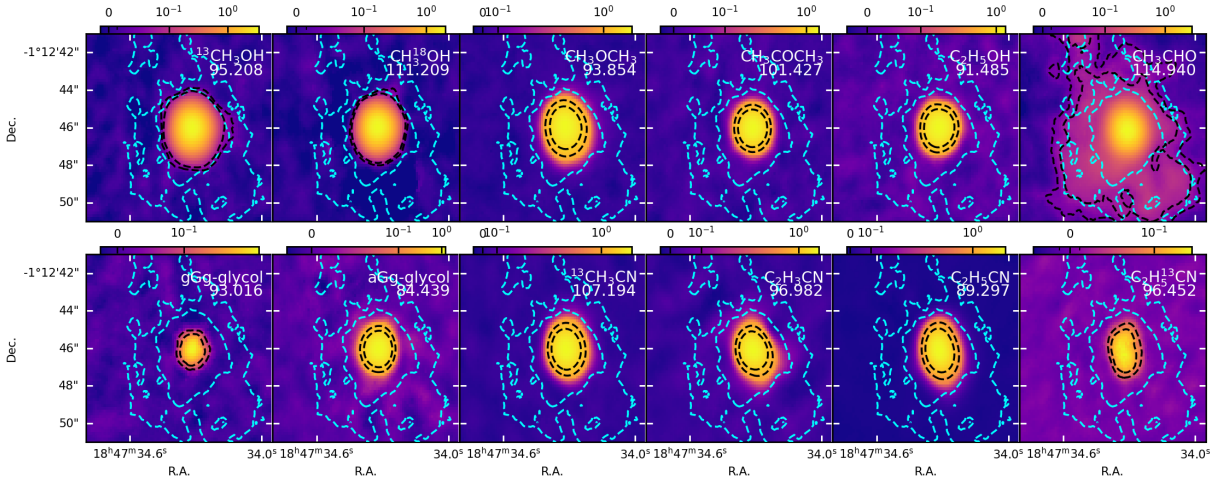

Fig. D.1. Moment-0 maps of low-energy transitions for the molecular species analyzed in this paper. We do not include CH_3OH vt=1, CH_3CN v8=1, and $CH_3^{13}CN$ since there were no available transitions with $E_U/\kappa_B < 30$ K. The moment-0 maps are not normalized to the peak intensity (i.e., to 1, as done for the mean maps shown in Fig. 1). The units are Jy/beam km s^{-1}. The black dashed contours are the 5rms and 10rms contour of the color-scale image, while the cyan dashed contours are the 5rms and 10rms contours of the mean map of CH_3CHO shown in Fig. 1.